USGS Award No. G13AP20027

REMOTE SENSING MEASUREMENTS OF LIQUEFACTION-INDUCED GROUND DEFORMATION FROM THE 2011 TOHOKU EARTHQUAKE

FINAL TECHNICAL REPORT

SUBMITTED: June 2014

ELLEN M. RATHJE, PH.D., P.E.
University of Texas at Austin
ECJ 9.227C, C1792
Austin, TX 78712
Tel: 512-232-3683
Fax: 512-471-6548
e.rathje@mail.utexas.edu

AWARD PERIOD
June 2013-May 2014

Research supported by the U.S. Geological Survey (USGS), Department of the Interior, under USGS award number (G13AP20027). The views and conclusions contained in this document are those of the authors and should not be interpreted as necessarily representing the official policies, either expressed or implied, of the U.S. Government

ABSTRACT

Liquefaction-induced deformations associated with lateral spreading represent a significant hazard that can cause substantial damage during earthquakes. The ability to accurately predict lateral-spreading displacement is hampered by a lack of field data from previous earthquakes. Remote sensing via optical image correlation can fill this gap and provide data regarding liquefaction-induced lateral spreading displacements. In this report, liquefaction-induced deformations from the 2011 Tohoku earthquake and 2011 Christchurch earthquake are measured using optical image correlation applied to 0.5-m resolution satellite imagery. The Christchurch earthquake is analyzed in addition to the Tohoku earthquake because the Christchurch has better documentation of the extent of liquefaction and lateral spreading. For both earthquakes, the resulting deformations from optical image correlation compared well with field observations of liquefaction and measurements of deformation.

1.0 INTRODUCTION

During earthquakes, loose, saturated soils may lose strength in a phenomenon known as liquefaction. Liquefaction manifests itself in many ways including slope failures, foundation failures, extreme settlement, sand boils, and lateral spreads. Lateral spreads occur as soil on a gentle slope or river bank liquefies and flows downslope or into the river, often developing cracks perpendicular to the direction of movement and causing extensive damage. Lateral spread deformation can cause significant damage to overlying infrastructure such as roads, bridges, buildings, as well as subsurface infrastructure like pipelines, utilities, and tunnels. Figure 1.1(a) shows a lateral spread from the 2010 Haiti Earthquake. Extensive cracking is oriented perpendicular to the waterway, and the depth of the affected soil is significant. Both overlying structures and subsurface infrastructure were affected by these deformations. Although this spread terminates within 50 meters of the waterway, lateral spreads may extend further inland for a few hundred meters. For example, the lateral spread in Figure 1.1(b) covers a much larger area. Again, cracking runs roughly perpendicular to the waterway. Extensive damage to the round structure, parking lot, roadways, and surrounding areas is clearly visible, and a large crack extends through the center of the structure's foundation.

Due to the complex nature of lateral spread mechanics, empirical models are typically used in practice to assess an area's susceptibility to lateral spread deformation and predict displacements in the event of an earthquake. More advanced numerical models derived from finite element analyses and theoretical liquefaction mechanics exist as well. However, all methods are limited by the quantity, quality, and accuracy of the lateral spread measurements used to develop or calibrate the models.

Traditionally, lateral spread displacement is measured manually using the widths of the cracks associated with lateral spreading. For example, if a lateral spread has occurred near a river, the widths of cracks running perpendicular to the orientation of displacement are measured, typically with a tape or GPS measurements on either side of the crack. Figure 1.2 illustrates the typical measurement of lateral spread induced cracking. Only cracks caused by the lateral spread are measured, and these crack widths are summed to determine the displacement of the lateral spread. However, this approach assumes that all lateral spread deformation is manifested in cracks and that the materials between cracks act as rigid blocks.

(a) (b)

Figure 1.1. Examples of Lateral Spreading

(a) Measurement of Crack using Tape

(b) Measurement of Crack with GPS

Figure 1.2. Traditional Measurement of Lateral Spreads (Robinson et al. 2011)

Such manual measurements present many challenges. They are time consuming and labor intensive. Assessment of only a few kilometers along a river may take weeks to perform, even with a sizable crew. The time and labor requirements translate to high costs. Additionally, the large spatial extent of many lateral spreads causes difficulty in determining the termination of lateral spread induced cracking. At far distances from the toe of the spread, visible cracking may not be due to lateral spreads, but other earthquake related phenomena. Accessibility of obstructed areas can be an issue with manual measurement as well. Last, recognition of cracking and the determination of crack widths are often difficult. Cracks may be hidden under debris or sand boils, and cracks which can be seen may not have an obvious cause. After determining a crack is associated with a lateral spread, the measurement of its width requires judgment and skill. For example, the width may be overestimated if the sides of the crack have slumped.

Measurements of deformation using optical image correlation can mitigate these challenges. In optical image correlation, a pre-earthquake image of an affected area is compared with a post-earthquake image of the same area. A map of lateral displacements is produced from this comparison, and lateral spread displacement measurements can be determined from this map. A single person can perform a correlation analysis of images covering over 30 km^2 in just a few days, which is must faster than field measurements. Additionally, a pair of 0.5 m resolution satellite images can be purchased for less than $500, making this approach cost effective. Imagery of areas which are inaccessible in the field may be attainable with satellites or aerial photography. Because displacements derived from this method are based on identifying homologous areas, measurements are not dependent on judgments of cracking patterns and widths. With optical image correlation techniques, existing databases of lateral spreading measurements can be expanded and diversified to include lateral spread deformation measurements that traditional techniques are unable to capture. With better displacement databases, better models can be developed for assessing lateral spread susceptibility, predicting lateral spread displacements, and mitigating lateral spread potential.

The research applies optical image correlation to measure displacements due to lateral spreading from the 2011 Tohoku earthquake in Japan. Before analyzing imagery from the Tohoku earthquake, we analyze imagery from the February 2011 Christchurch Earthquake in New Zealand. This preliminary analysis was used to refine the analysis techniques for an area where deformations and liquefaction were well-documented.

2.0 OPTICAL IMAGE CORRELATION

The optical image correlation process can be divided into three categories: (1) pre-processing, (2) correlation analysis, and (3) post-processing. A flow chart of the process is shown below in Figure 2.1. In pre-processing, an image pair is selected and distortions in the images are corrected through orthorectification and co-registration. During the correlation analysis, displacements are determined. Finally, in post-processing, the results are filtered and derivative products such as transects, vector maps, and displacement contour maps are created from the correlation results.

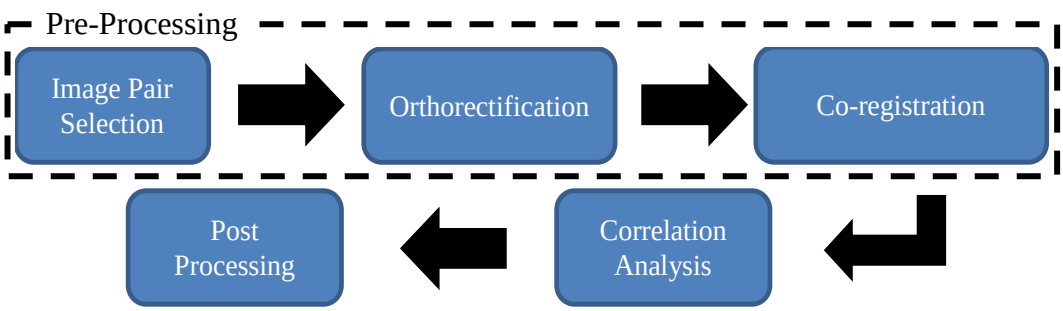

Figure 2.2. Image Correlation Process Flow Chart

2.1 Image Pair Selection

The properties of the selected images have the greatest influence on the quality of results. Images are selected on three main criteria: (1) coverage, (2) cloud cover, and (3) acquisition geometry. Images must contain the region of interest and surrounding areas. A significant area surrounding the region of interest is required because these areas are used in the co-registration process to reduce distortions. Additionally, images must be free of significant cloud cover near the region of interest. Last, but certainly not least, the acquisition geometry must be favorable.

The acquisition geometry describes the location of the optical sensor relative to the location of the target image on the surface of the earth. Typically, the acquisition geometry is described using one of two parameter sets: (1) the off-nadir (i.e., off-vertical) and azimuth angles or (2) the sensor's path azimuth, cross-track, and in-track angles. Figure 2.2 illustrates the angles used to describe the line-of-sight from an optical sensor on a satellite to a point in an image (i.e. a pixel). Using the first parameter system, the off-nadir angle is represented by ϕ_L and the azimuth angle is θ_L. The second parameter system is referenced by T, S, and θ_0, which represent the cross-track, in-track, and orbital path azimuth angles, respectively. Note that the azimuth angles in both systems are measured clockwise from north. These angles are related by the following equations.

$$\tan(\phi_L) = \sqrt{\tan^2 S + \tan^2 T} \tag{2.1}$$

$$\tan(\theta_I) = \frac{\tan(S)}{\tan(T)} \tag{2.2}$$

$$\theta_L = \theta_I + \theta_0 \tag{2.3}$$

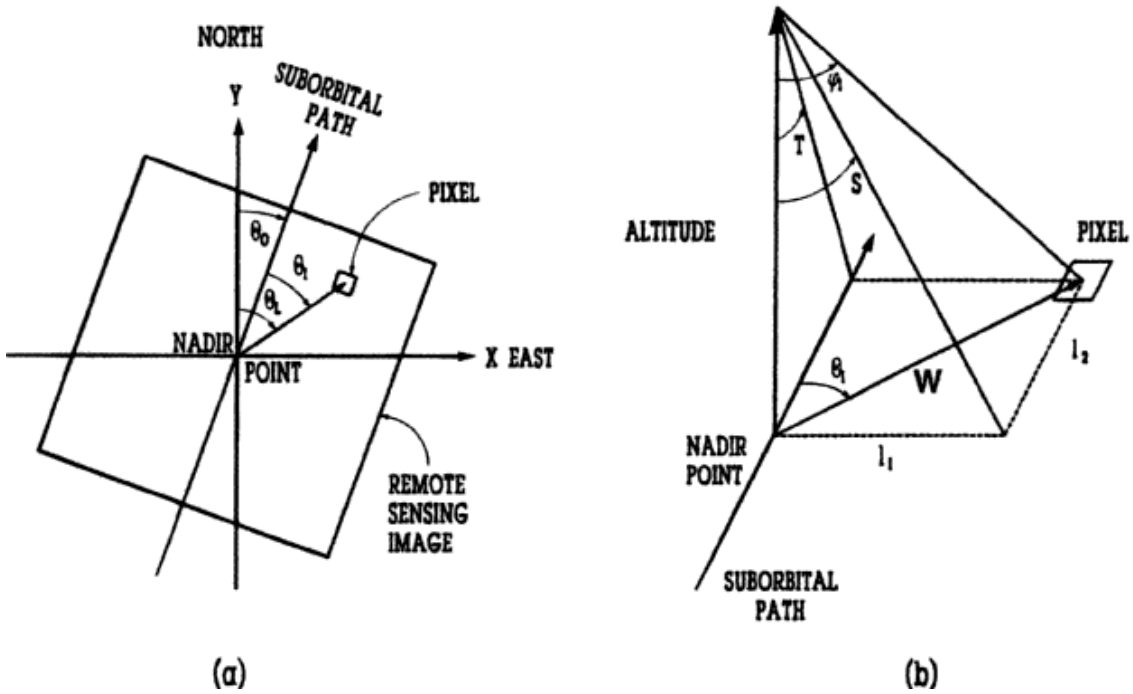

Figure 2.3. Acquisition angles from (a) plan view and (b) isometric view. Note: (b) shows angles referenced from the satellite orbital path (Bukata 1977)

Two important considerations must be made regarding acquisition angles when selecting image pairs. First, the off-nadir angle should be minimized because distortions due to the topography of the target area are greater when the off-nadir angle is greater. Second, the acquisition angles of the pre-event image should be similar to those in the post-event image. As the acquisition angles differ more from each other, apparent (not true) displacements may be obtained from the analysis. Additionally, patterns of pixels are more easily identifiable if the post- and pre-event images are captured from the same perspective.

2.2 Orthorectification

Orthorectification corrects for geometric distortions such as relief displacement to generate a nadir (i.e., vertical) view of the target. Relief displacement is the difference in the perceived position of an object from its actual position due to parallax. Figure 2.3 illustrates relief displacement of an office building. Because the building is viewed from an angle, its roof is incorrectly placed. Figure 2.4 shows two images in which the effects of relief displacement are clearly visible. The top of the water tower appears in different locations depending on the acquisition angle of the image. Relief displacement is magnified when an object is viewed at a greater off-nadir angle and when topographic variation is larger.

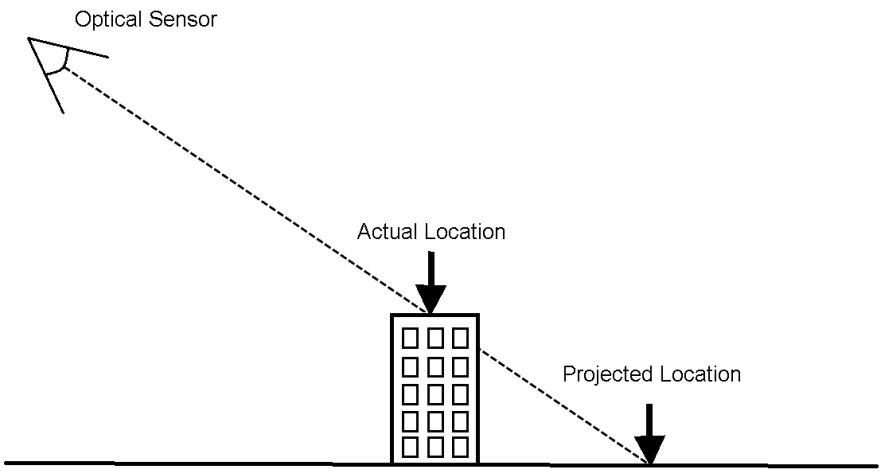

Figure 2.4. Relief displacement due to off-nadir angle.

L R

Figure 2.5. Relief displacement of top of water when viewed from left and right of tower. (Bethel 2014)

Another common geometric distortion is one of scale. Figure 2.5 (a) shows a profile view of an area with three equally sized features. Without geometric corrections, object (2) will appear smaller than the other objects because it is further away (Figure 2.5b). After orthorectifying the image, all three objects are the same size (Figure 2.5c).

Orthorectification uses a digital elevation model (DEM) of the ground surface and an image's acquisition angles to correct geometric distortions. Typically, the DEM resolution is coarser than the distorted image, so all distortions are not removed through orthorectification. Additionally, some distortions of buildings are not removed because the elevations of buildings are not included in the DEM.

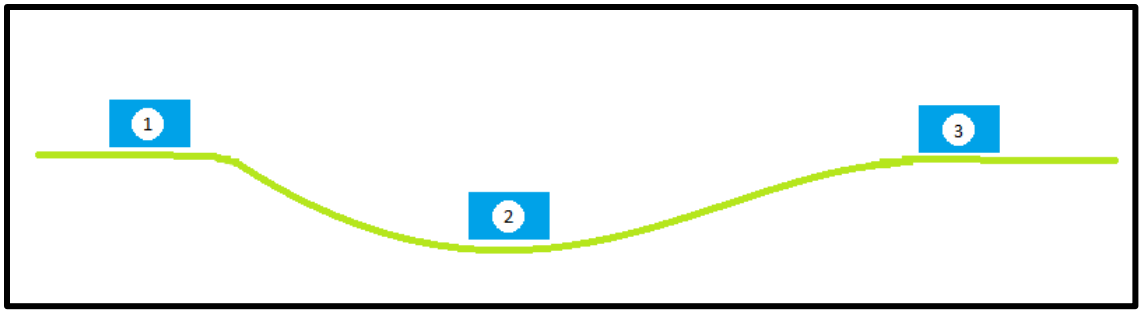

(a) Profile view

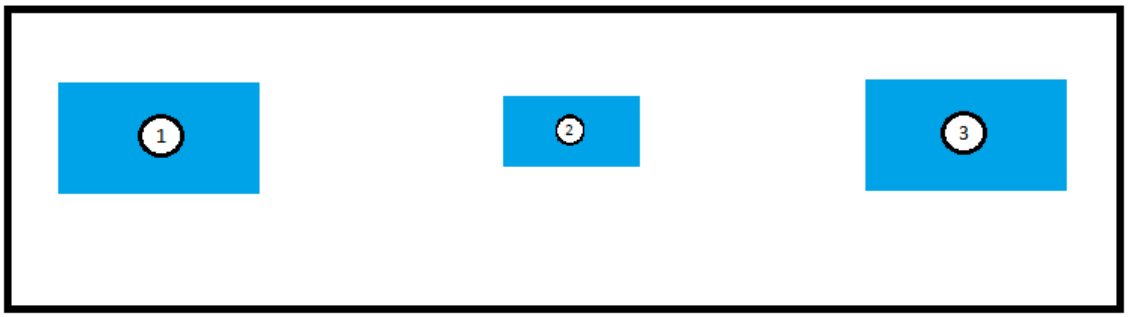

(b) Plan View – Pre-orthorectification

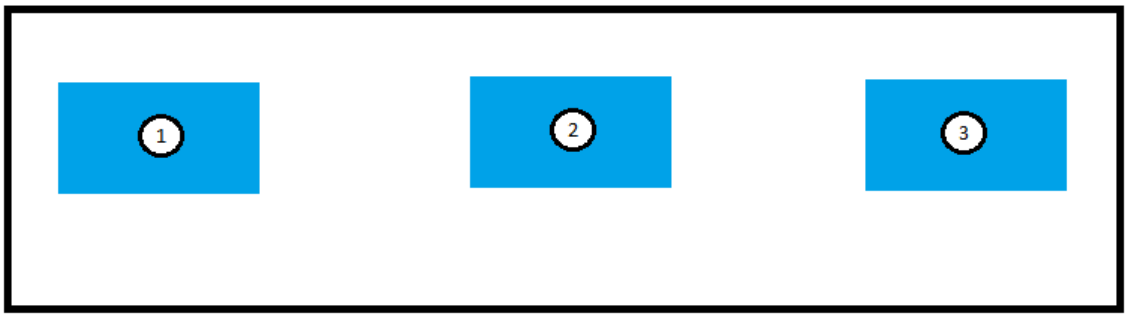

(c) Plan View – Post-orthorectification

Figure 2.6. Using orthorectification to correct scale: (a) profile view of area with three equally sized features, (b) plan view of acquired image before orthorectification, and (c) plan view after orthorectification.

2.3 Co-registration

Co-registration involves precisely aligning the pre- and post-event images. Distortions and geo-referencing errors that remain after orthorectification are mitigated through co-registration. Co-registration warps the post-event image so that defined tie points (i.e., homologous points between the images) are at the same location when overlaid. The post-event image is warped using a first order polynomial that is fit with selected tie-points.

Tie points are generated using an automated process in which groups of pixels in the pre-event image are compared with those in the post-event image. While the specific implementation of the automatic tie-point generation may vary, most area-based tie point

generation processes are similar to that which is illustrated in Figure 2.6 and described in Gao et al. (2009). A given group of pixels (chip window) in the pre-event image (red box in Figure 2.6) is compared to multiple groups of pixels in the post-event image (green and orange boxes in Figure 2.6). For each comparison, a correlation coefficient is calculated to reflect the quality of match. The post-event chip window with the highest correlation coefficient is assumed to match the pre-event chip window. This process is repeated at multiple locations to obtain tie-points.

Automated tie-point generation methods work well in areas with unique features that manifest themselves in variations in pixel values or texture (e.g. urban areas). However, these methods are less reliable in areas with few features or homogenous texture (e.g. rural areas with fields). Figure 2.7 illustrates the use of automated tie-point generation methods in areas with little texture (Figure 2.7a) and significant texture (Figure 2.7b). In this figure, the correlation coefficient is plotted again the location index, which represents the shift applied to the pre-event chip window within the post-event image. In Figure 2.7a, multiple locations potentially match the pre-event chip window, so a false positive is more likely. Conversely in Figure 2.7b, the pre-event chip window clearly matches one location in the post-event image. Therefore, the automated tie-point generation is more reliable in areas with unique features/texture.

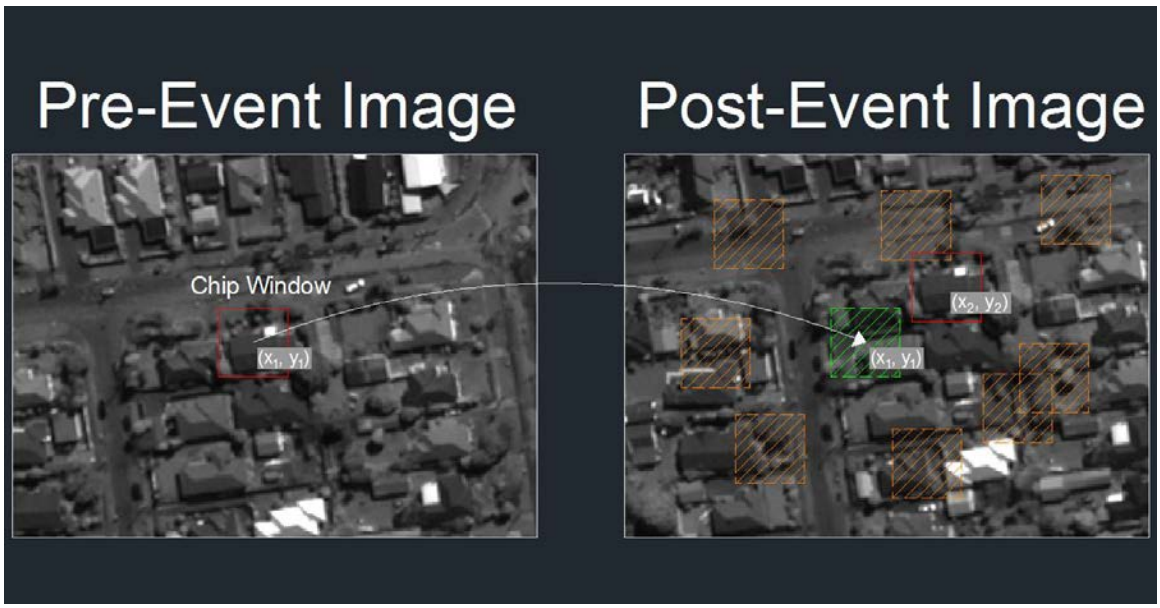

Figure 2.7. Optical Image Correlation Process.

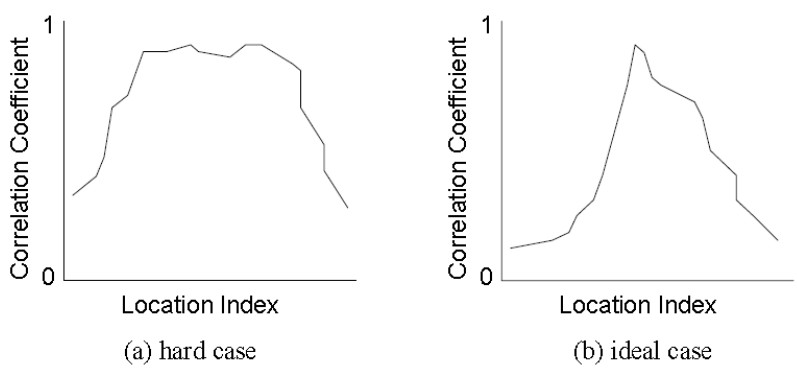

Figure 2.8. Comparison of automated tie point generation in two areas (Gao et al 2009).

Once tie-points have been generated, they are filtered to ensure the first order polynomial is fit using only appropriate tie-points. Tie points in areas of expected displacement (e.g. near rivers) are removed. Remaining tie points are assessed by fitting the first order polynomial with the points and calculating the residuals for each point. In addition, a root mean square error (RMSE) is determined for the entire fit and represents the scatter of all points about the best fit line. Because the first order polynomial can only account for distortions common throughout the whole image, tie points with high residuals are likely false positives or located in areas of localized deformation. Therefore, tie points with high residuals are removed until an acceptable RMSE is reached with an appropriate density and distribution of tie points.

2.4 Correlation Analysis

Correlation analysis provides estimates of displacement across an area in a process similar to that of the automated tie point generation described above. Figure 2.6 can be used again to illustrate the correlation analysis. The pre-event image is divided into patches of pixels, called chip windows. For each chip window in the pre-event image, a search is performed in the post-event image to find the location of the same chip. For example, the red square in the pre-event image (Figure 2.6) outlines a chip window centered at location (x1, y1). In the post-event image, the chip window first is compared to the pixels at the same (x1, y1) position (shown in green in Figure 2.6). The comparison is quantitatively measured with a correlation coefficient between the corresponding pixel values within the two chips. The chip also is compared to surrounding locations (illustrated by the orange squares in Figure 2.6), and a correlation coefficient is calculated for each location. The chip with the highest correlation (the red square in the post-event image in Figure 2.6) is considered the best match, and this location is taken as the location of the pre-event chip in the post-event image. A signal-to-noise ratio (SNR) is assigned to the match reflecting the quality of correlation (1 = perfect correlation; 0 = no correlation). The position of the best-match chip in the post-event image (x2, y2) is compared with the position in the pre-event image (x1, y1) to obtain relative east-west and north-south displacements. The correlation process has been shown to be accurate to 1/20 of a pixel using some algorithms (Leprince et al. 2007). Therefore, the precision of the displacement measurements is typically controlled by the precision of the co-registration process.

The selection of the chip window size significantly influences the pattern of results. A correlation measurement represents an average displacement across an entire chip window, and thus smoothing of displacement is greatest for large chip windows. Correlation using small chip windows produces less averaging and more localized estimates of displacement, but noisy, incoherent displacement patterns are more likely due to false matches. Therefore, the smallest chip window that produces an acceptable level of noise should be used. The spacing at which a new chip is compared is called the step size. A smaller step size produces more displacement measurements but is more computationally intensive.

2.5 Post-Processing

Post-processing involves filtering the displacement estimates by their SNR and creating derivative products from the correlation results. Displacement estimates under a specified SNR are removed such that only displacements from well-correlated chips are present. The minimum allowable SNR is determined based on the use of the end products.

The smallest detectable displacement magnitude should also be assessed during post-processing. As noted in the discussion on correlation analysis, the limiting precision typically

comes from the co-registration process. Specifically, the RMSE from the co-registration provides important information on the variability of displacement in non-moving areas. The RMSE essentially represents the scatter (i.e., standard deviation) of the tie points about the best-fit warping polynomial and thus is a measure of the variability of displacement in non-moving areas. Therefore, the RMSE can be used to estimate the minimum detectable displacement magnitude.

From the correlation results, many derivative products can be generated. Maps showing displacement in different directions (e.g. North/South and East/West directions) or as amplitude (i.e. square root of sum of components squared) can be created. Transects showing displacement versus distance from the riverbank and vector arrows can be derived from the correlation results. Even contour maps showing displacement concentrations are possible.

2.6 Previous Uses of Optical Image Correlation to Measure Deformations

Optical image correlation has previously been used in geotechnical and earthquake applications. Hamada et al. (1987) used two aerial photographs of Noshiro City, Japan to measure liquefaction induced lateral displacements from the 1983 Sea of Japan Earthquake. Hamada et al. (1987) compared an image taken in 1981 to one acquired seven days after the earthquake. They first aligned the images by identifying points in areas that were assumed to have no permanent displacement. Next, points in the moving areas were manually identified in both images to determine a relative displacement. Where possible, manhole covers, bases of lamp-posts, corners of drainage channels, and property boundary stones were used as reference points. When such objects could not be found, corners of buildings were used. Figure 2.8 shows some points used to measure permanent displacement on Maeyama Hill in Noshiro City. Once points were identified, they were assigned a location based on a coordinate system. By comparing the coordinate position of the object in the pre- and post-event images, the lateral displacement was quantified. Hamada et al. (1987) estimated the error in these measurements as being no greater than 20 cm. They used the same technique to estimate displacements near Niigata, Japan from the 1964 Niigata Earthquake.

With advances in computing technology, optical image correlation techniques are now automated. Many researchers have estimated earthquake fault rupture displacement using optical image correlation. Binet and Bollinger (2005) measured the fault displacement of the 2003 Bam (Iran) earthquake with a pair of SPOT-5 panchromatic images (2.5 m pixel width). They used the correlation technique described by Van Puymbroeck et al. (2000), which matches pre- and post-event areas through Fourier transforms. Figure 2.9 shows the area of their analysis and the correlation results. With a correlation window size of 256 pixels (640 m) and a step size of 64 pixels (160 m), they measured right lateral strike slip displacement of roughly 0.77 ± 0.05 m on average. Near the center of the fault rupture, their measurements showed a maximum displacement of 1.2 ± 0.15 m. These measurements were larger than field estimates (average field displacement was estimated at 0.2 m), but the authors believe the field estimates are under predictive because they only represent discrete rupture along the fault.

Figure 2.9. Location of lateral displacement measurements near Noshiro City, Japan; measured points shown as circles (Hamada et al. 1987).

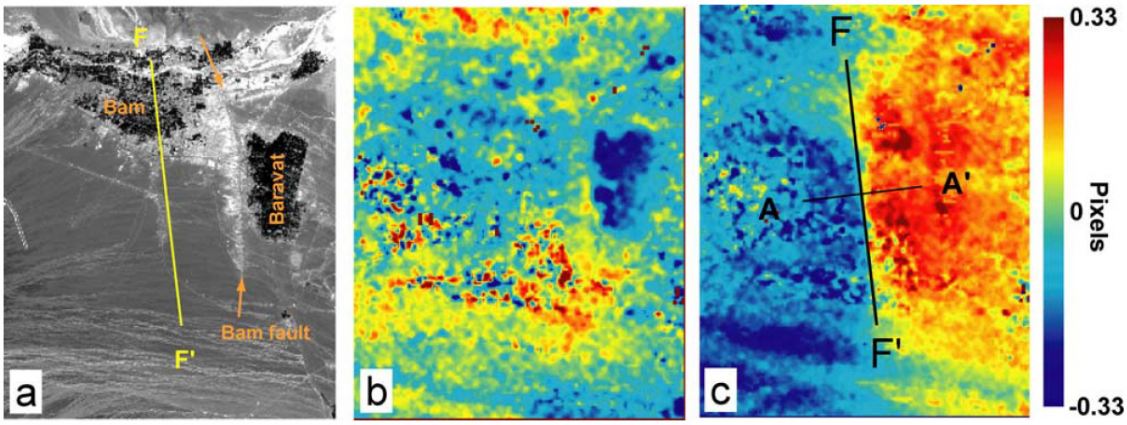

Figure 2.10. Image and map of displacements induced by Bam (Iran) earthquake: (a) SPOT optical image, (b) east/west component of displacement, and (c) north/south component of displacement. Note the fault displacement along F-F' is clearly visible (Binet and Bollinger 2005).

Debella-Gilo and Kääb (2012) used an area-based optical image correlation process (Least Squares Matching (LSM) algorithm) to assess displacement and strain rates of three mass movements: a glacier flow, a rockglacier creep, and a landslide. While the correlations for the glacier flow and rockglacier creep yielded positive results, only the land slide analysis will be discussed in detail as it most closely relates to the topics in this thesis. Two Quickbird satellite

images from September 2003 and September 2010 were analyzed to determine the displacement and seven-year average velocity of the La Clapière landslide in the French Alps near the town of Saint-Etienne-de-Tinée. Figure 2.10 shows a portion of the 2003 Quickbird image. These images have a pixel resolution of 0.6 m, and the co-registration process yielded a mean error of about 1.2 m, or 2 pixels. Using a window size of 51 pixels (30.6 m), displacements were calculated. Figure 2.11 shows the correlation results. The spatial pattern of displacement agrees with results from other studies, particularly with the results of Casson et al. (2003) where points were manually compared in two stereoscopic aerial images acquired 17 years apart. While the spatial pattern of displacement from Debella-Gilo and Kääb (2012) compared well with other studies, uncertainty in the displacement measurements was high. Specifically, the average displacement measured outside the landslide area (i.e. non-moving areas) was 2.01 pixels (1.2 m), so calculated displacement measurements were within the error margin. Therefore, the reliability of the displacement magnitudes is questionable. Since the mean precision of the LSM algorithm was found to be within 0.06 to 0.15 pixels (0.04 to 0.09 m), the uncertainty in measurements was controlled primarily by errors in the co-registration process.

Figure 2.11. Quickbird Image of La Clapière landslide from 2003 (Debella-Gilo and Kääb 2012).

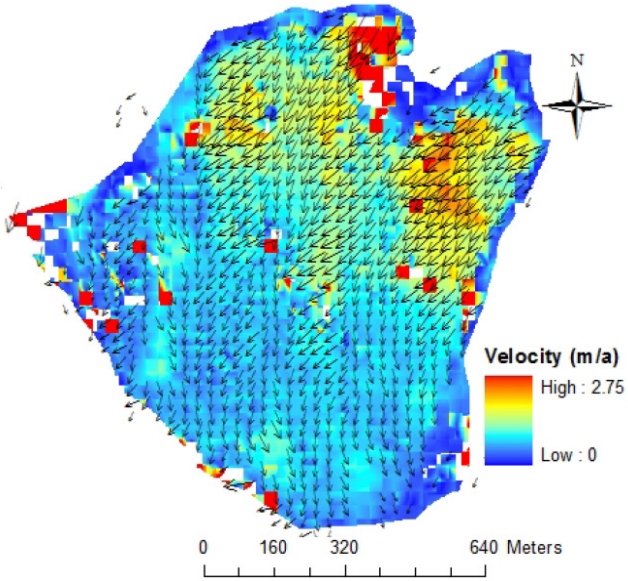

Figure 2.12. Displacement rate results of La Clapière landslide correlation (Debella-Gilo and Kääb 2012).

Suncar et al. (2013) measured the displacement of the Portuguese Bend landslide in Los Angeles County using the optical image correlation process discussed in Leprince et al. (2007). Figure 2.12 shows the location of the landslide. Correlating two panchromatic images with 0.5 m pixel resolution acquired in August 2010 and May 2011 with a 128 pixel (64 m) window size, they determined the magnitude and extent of landslide deformations and compared their results to measurements from 64 GPS benchmarks within and around the landslide area. Figure 2.13 shows the deformation results along with those inferred from GPS measurements. Displacements from 0.5 m to greater than 6 m were measured. Measurements from optical image correlation agreed well with GPS measurements and provided a more coherent deformation pattern than could be derived solely using the GPS measurements.

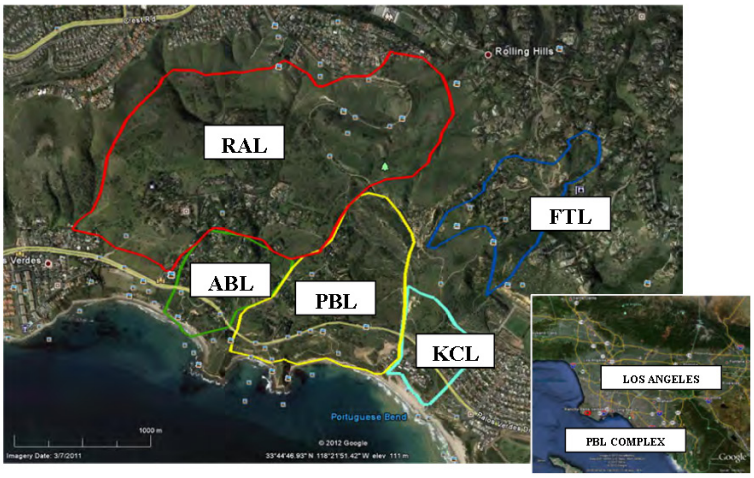

Figure 2.13. Location of Portuguese Bend Landslide (PBL) (Suncar et al. 2013)

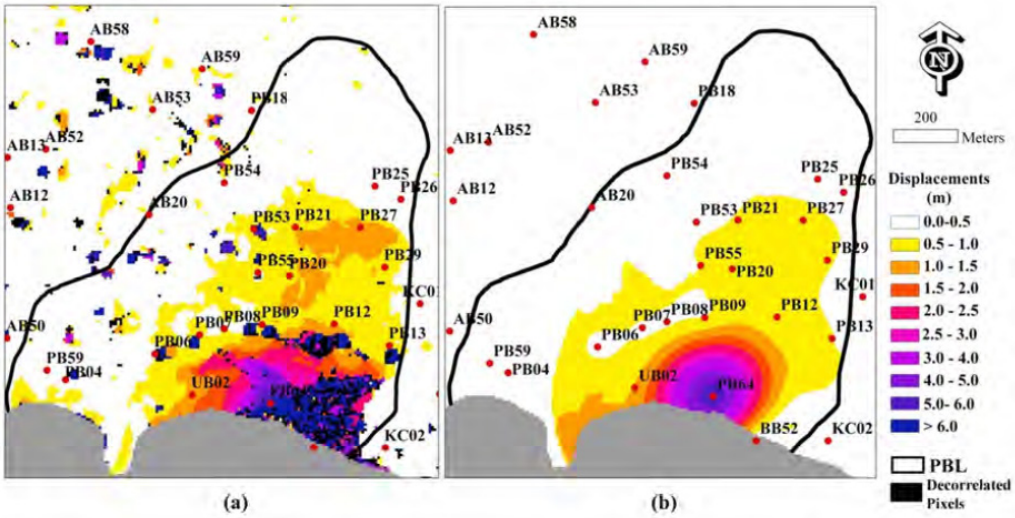

Figure 2.14. Comparison of displacement patterns: (a) displacements from optical image correlation and (b) displacements from GPS measurements. Note: the precision in defining the landslide geometry is greater with the optical image correlation results (Suncar et al. 2013).

3.0 OPTICAL IMAGE CORRELATION ANALYSIS OF LIQUEFACTION FROM THE 2011 CHRISTCHURCH EARTHQUAKE IN NEW ZEALAND

3.1 Study Area

On February 22, 2011, a M_w=6.3 earthquake occurred near Christchurch, New Zealand severely damaging infrastructure and claiming 181 lives (Cubrinovski et al. 2011). Figure 3.1 shows the city of Christchurch, surrounding neighborhoods, and the epicenter of the earthquake. Much damage was caused by severe liquefaction and lateral spreads in and around the Christchurch Central Business District (CBD) and surrounding neighborhoods. In particular, lateral spreading due to liquefaction caused permanent horizontal displacements of more than 2 m in the neighborhoods along the Avon River to the east of the CBD (Cubrinovski et al. 2011). Figure 3.2 shows a lateral spread in a surrounding neighborhood of Christchurch. The lateral spread caused permanent displacement toward the Avon River, and the affected areas were severely damaged. Because of the significant documentation of the lateral spread displacements in Christchurch, optical image correlation was applied first to this study area before moving on to the Tohoku earthquake (Chapter 4).

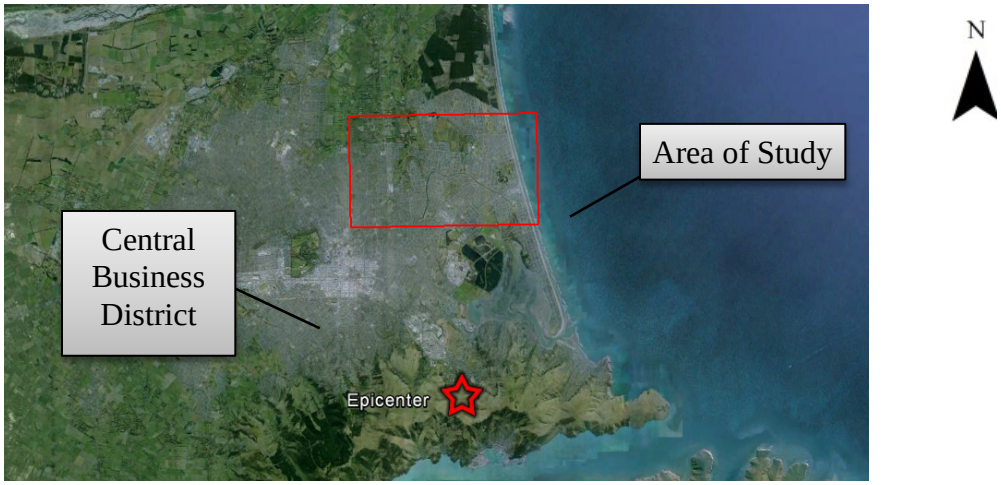

Figure 3.15. Area of study for the February 2011 Christchurch Earthquake (Google Earth 2014).

Figure 3.16. Lateral spread toward Avon River in Christchurch, NZ (Cubrinovski et al. 2011).

3.2 Image Selection and Processing

Given the severity of liquefaction induced horizontal displacements and availability of satellite imagery, an area encompassing the neighborhoods along the Avon River to the east of the CBD was selected for study. The area of study is outlined in red in Figure 3.1. The near surface soils in this area consist of fine sands and silty sands deposited by fluvial processes, and the upper 5-6 m of soil is very loose. Additionally, the water table is approximately 1 m below the surface (Cubrinovski et al. 2011).

Pre- and post-earthquake images from the 2011 Christchurch earthquake were selected based on their similar acquisition angles and 0.5 meter pixel resolution. These panchromatic (i.e., gray-scale) images were collected by the WorldView-1 (pre-event) and GeoEye-1 (post-event) satellites. The pre- and post-earthquake images were acquired on September 21, 2010 and February 26, 2011, respectively, with off-nadir angles of 19.8° and 18.2° and target azimuths of 55.1° and 51.1°, respectively. Importantly, the pre-event image was acquired after the September 3, 2010 Darfield earthquake. Figure 3.3 shows the pre-event image with the location of neighborhoods indicated that will be discussed in detail later.

By using equations 2.1, 2.2, and 2.3 and assuming a pseudo-suborbital path of 0° (i.e. $\theta_0 = 0$), north/south look angles (T) of 11.64° and 11.67° and east/west look angles (S) of 16.45° and 14.35° can be established for both the pre- and post-event image, respectively. The difference in the north/south look angles is 0.03°, and the difference in the east/west look angles is 2.10°. These differences in acquisition angles are small enough that there should not be noticeable displacement signatures associated with DEM errors, etc.

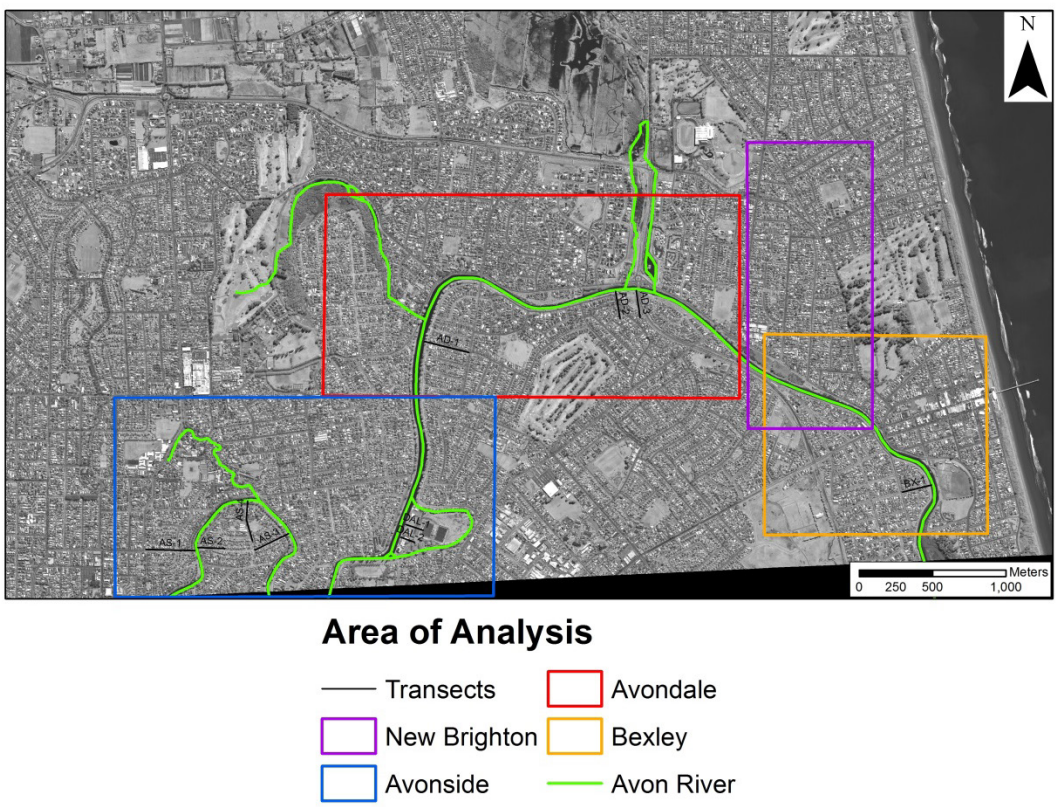

Figure 3.17. Pre-event (Sept. 21, 2010) satellite image and neighborhoods of interest.

The two images were orthorectified using open source software GDAL (Geospatial Data Abstraction Library, GDAL 2012) and a digital elevation model (DEM) of 90 m resolution from the Shuttle Radar Topography Mission (SRTM, USGS 2004). Next, tie points were generated for co-registration using the software ENVI (ENvironment for Visualizing Images, ENVI 2014). ENVI generates tie points automatically using normalized cross correlation to identify corresponding locations in the two images (EXELIS 2013). Tie points identified within 300 m of the river were discarded because lateral spreading movements were expected within this zone and therefore these locations should not be tied between the two images. Additionally, tie points with large residuals relative to the warping polynomial were removed because (1) large residuals potentially indicate false-positive tie points (i.e., the areas identified in the two images are not the same) and (2) the first order polynomial should not correct for localized differences in the images. Figure 3.4 shows all the tie-points generated from ENVI's automatic tie point generation tool overlaid with correlation results (performed later) near the Avondale neighborhood. Points which were discarded are displayed as red x's, while selected tie points are represented with colored circles. Note that most tie-points near areas of large displacement were discarded and the few remaining tie-points in these have higher residuals because the warping polynomial does not account for localized deformation. This observation validates the use of tie point residuals as selection criteria. Ultimately, a density of 47 tie points per square kilometer was obtained, and 1,700 well-distributed tie points were used in the co-registration. The resulting RMSE across the image was 0.30 m. Figure 3.5 shows the tie points selected for post-event image warping with the residual of each tie-point represented by its color.

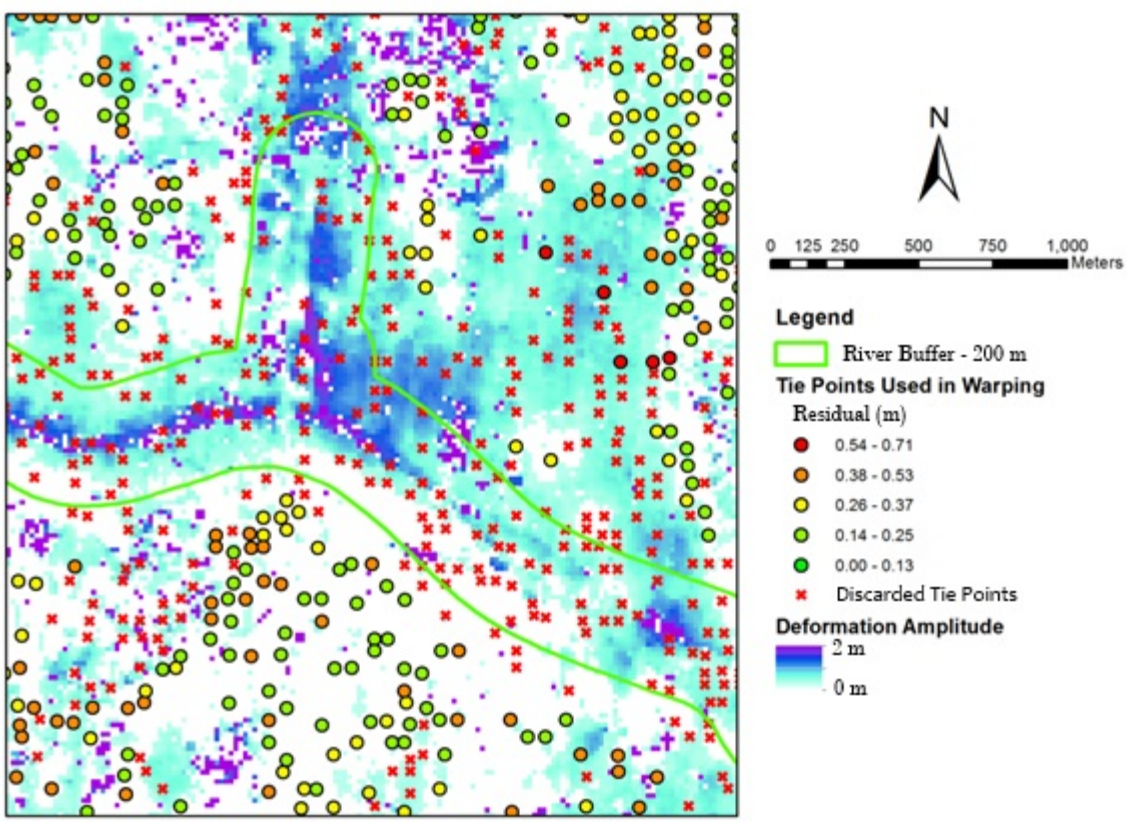

Figure 3.18. Tie point locations compared with deformation results.

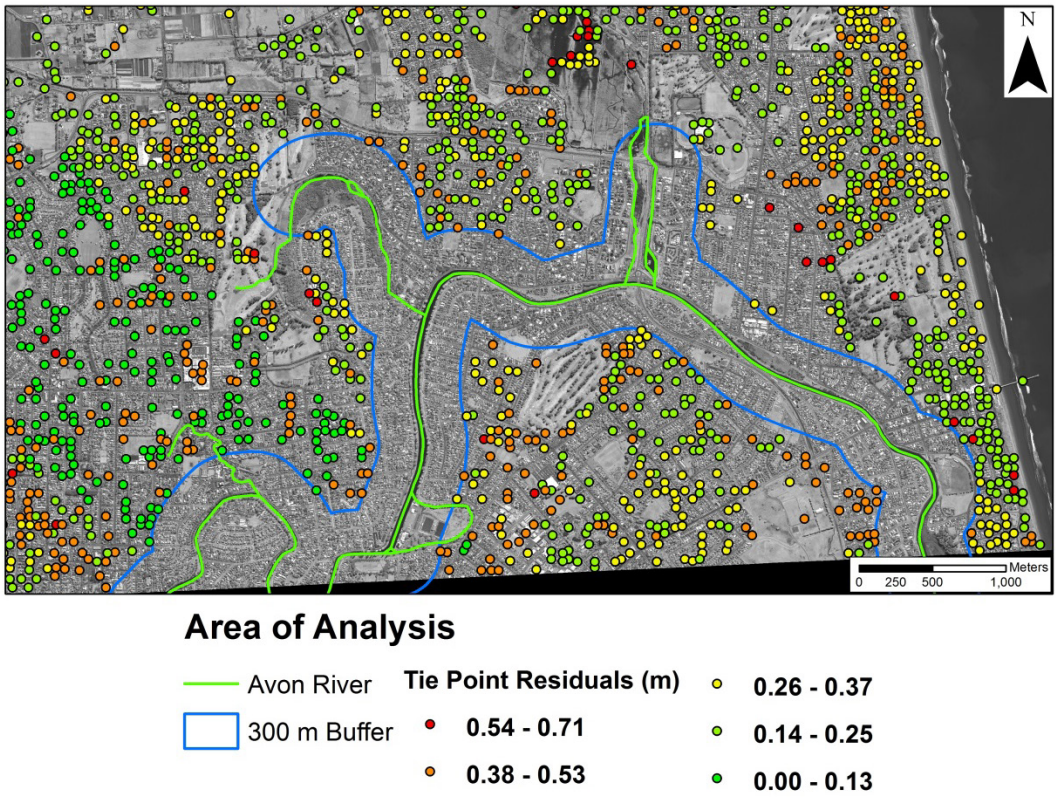

Figure 3.19. Tie points selected for post-event image warping.

After co-registration, optical image correlation was performed using the program COSI-Corr (Leprince et al. 2007). A chip window of 128 by 128 pixels (64 m) was used with a step size of 32 pixels, which produced a displacement estimate every 16 m. Results with an SNR less than 0.95 were removed as "decorrelated" pixels. A precision displacement threshold of 0.30 m was established that represents the potential variation between the measured and actual displacement, as well as the smallest displacement that can be confidently distinguished from zero. The precision threshold value of 0.30 m was determined from the co-registration RMSE of 0.30 m, which dominates other sources of error, as discussed in Section 2.2.4. This threshold can also be estimated by examining measured displacements in non-moving areas (e.g. Debella-Gilo and Kääb 2012). Non-moving areas are areas where displacements measurements should be zero. Therefore, areas where coherent patterns of deformation are detectable or where correlation techniques are not expected to work (e.g. in bodies of water or in a large grass field) are excluded from statistical analysis of non-moving areas. Figure 3.6 shows frequency-distribution histograms of (a) north/south and (b) east/west displacements in non-moving areas from correlation analysis (results presented later). Each bin width is 0.02 m, and the center value of each bin is shown on the x-axis. The histogram of the north/south displacements indicates the mean displacement is close to zero (0.013 m) and 68% of the correlation measurements are within ± 0.164 m of the mean. Similarly, the histogram of the east/west displacements indicates the mean displacement is nearly zero (0.037 m) with 68% of the measurements occurring within ± 0.229 m of the mean. The square root of the sum of the squares of these standard deviation values is equal to 0.28 m. Thus, the statistics of the correlated displacements in non-moving areas confirm that the threshold, or precision, of the displacement measurements is about 0.30 m.

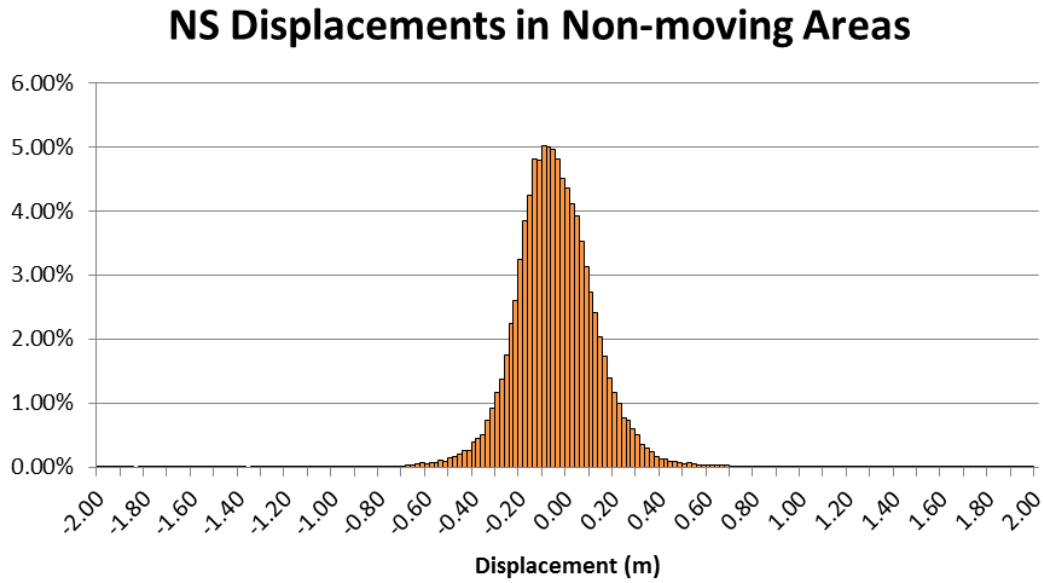

(a)

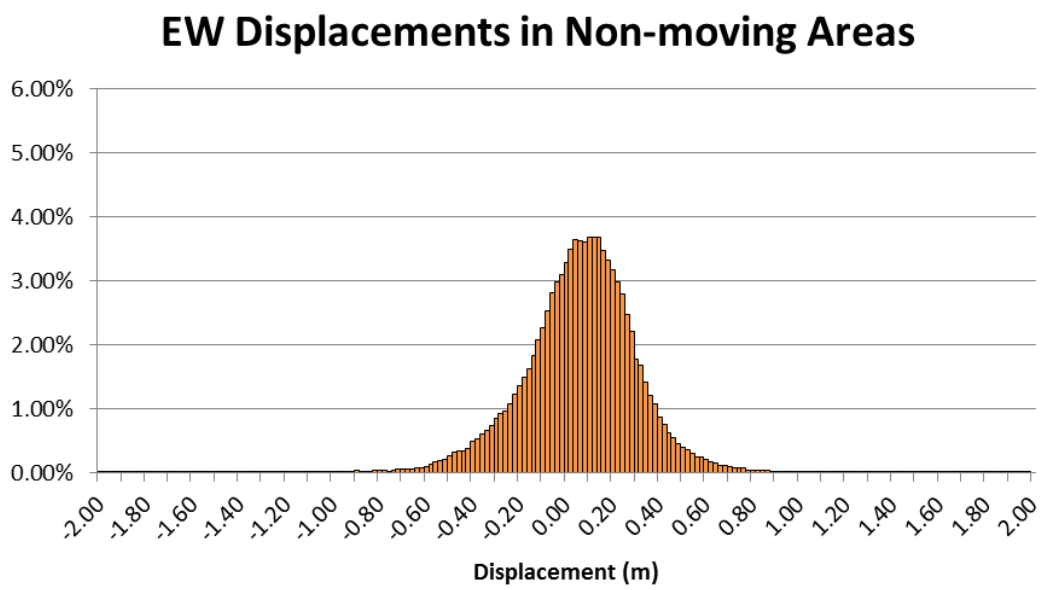

(b)

Figure 3.20. Histogram of (a) north/south and (b) east west displacements in non-moving areas.

3.3 Deformation Results

Displacements were measured in the north-south and east-west directions using optical image correlation. Figure 3.7 shows the amplitudes of the north-south displacements across the study area. Displacements less than the precision threshold were set to zero for visual purposes. Movements towards the north are shown in red/yellow, and movements towards the south are shown in blue/purple. Coherent zones of deformation are concentrated along the river with most displacement occurring within 150 m of the river. However, the lateral spread in the New Brighton area (purple box) extends further than 500 m from the river and would be difficult to define using traditional measurement techniques. North-south movements are largest in areas where the river runs directly east-west due to spreading towards the river. As expected, areas north of the river displace southward, while areas south of the river displace northward. This change in displacement direction from north to south at the river indicates that the deformations are associated with lateral spreading towards the river. The largest north/south displacements are on the order of 2 m or more (red areas).

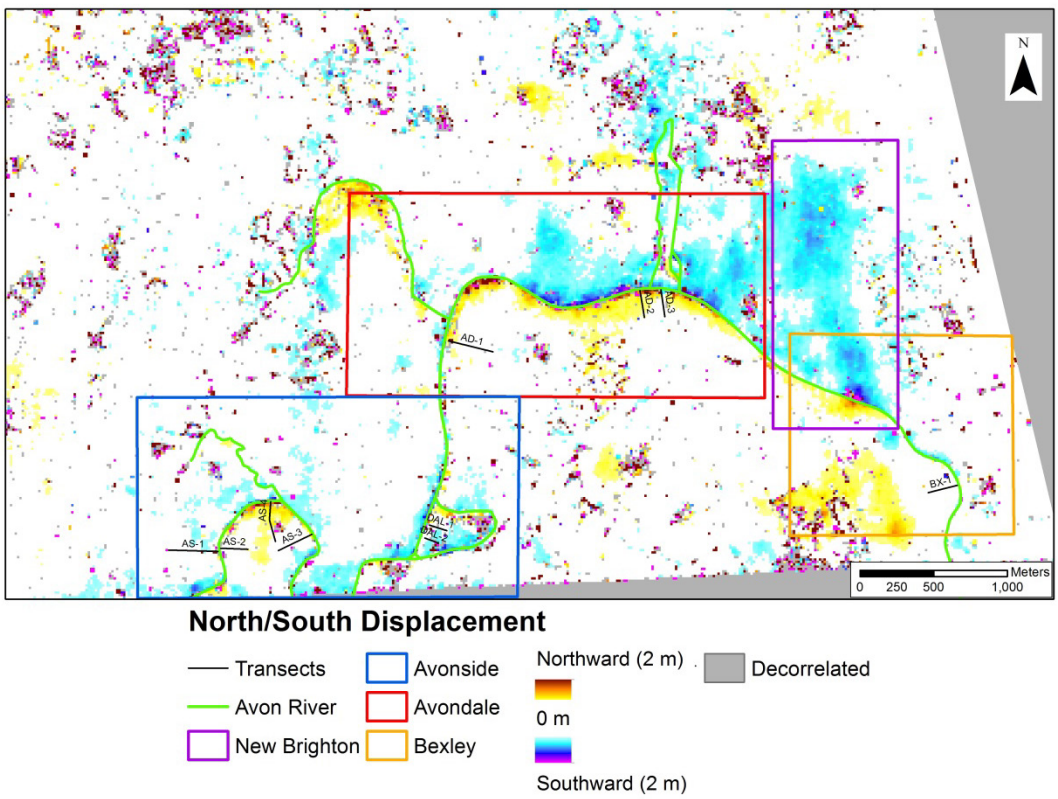

Figure 3.21. Overview of north/south displacements from correlation results

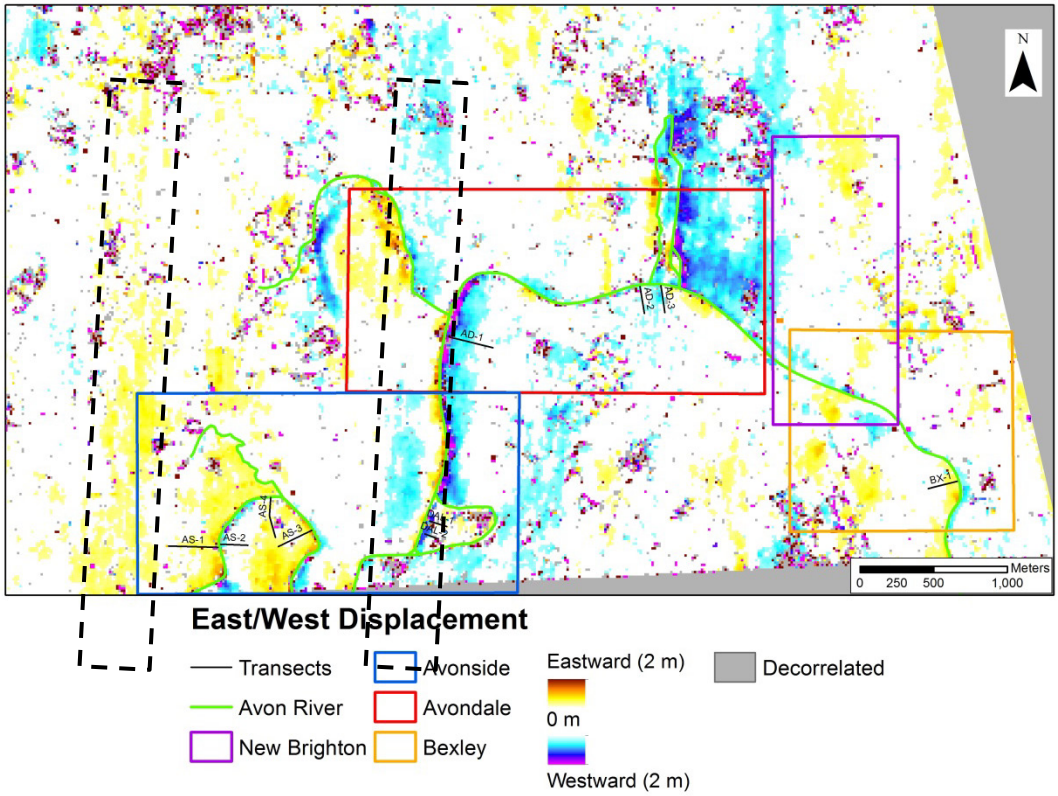

Figure 3.22. Overview of east/west displacements from correlation results.

Deformations in the east-west direction are shown in Figure 3.8 with red/yellow used for the eastward displacements and blue/purple for the westward displacements. Displacements less than the precision threshold were set to zero for visual purposes. Areas to the west of the river displaced predominantly eastward, and areas to the east of the river moved predominately westward, indicating lateral spreading towards the river. The largest displacements occur immediately adjacent to the river. There are significant lengths of the river that experienced 2 m or more of displacement (red and purple areas). These large east/west displacements are focused predominantly where the Avon River runs north/south in the eastern parts of Avonside and in the eastern parts of Avondale where the river splits.

Two areas outlined by the dashed lines display unexpected displacement patterns. These areas show strips of displacement that are independent from the river location. The distinct linear patterns of the displacement are likely banding artifacts from misalignment in the image acquisition. Pushbroom sensors on the satellites (including Worldview-1) use a linear array of detectors to collect image data (Krause 2008), and the data collected from each detector must be aligned to produce the full image. If the data are slightly misaligned, linear artifacts may be present in the correlation results as seen in the east/west displacements. While some of these artifacts were removed in the co-registration, not all were removed.

Comparisons of the measured displacement with qualitative and quantitative measurements of liquefaction displacements from other sources are discussed in the next sections. The results are examined for the four areas of interest identified in Figure 3.7 and Figure 3.8 so that detailed deformation patterns may be discussed more easily.

3.3.1 Comparison with Qualitative Lateral Spreading Observations

Ground observations of liquefaction and lateral spreading were collected in residential areas across Christchurch (Canterbury Geotechnical Database 2013). Observations were organized into three categories: (1) no liquefaction, (2) liquefaction, and (3) liquefaction and lateral spreading. These three categories were subdivided based on severity. A diagram illustrating these categories is shown in Figure 3.9. These observations only account for liquefaction with visible evidence at the surface. Not all properties were assessed before an aftershock occurred in June 2011, so the observations are somewhat incomplete. Also, it is possible that observations made after the February 2011 earthquake may include damage from the September 2010 Darfield Earthquake. Despite these uncertainties, the observations provide the best qualitative assessment of the severity of liquefaction across Christchurch for comparison to correlation results.

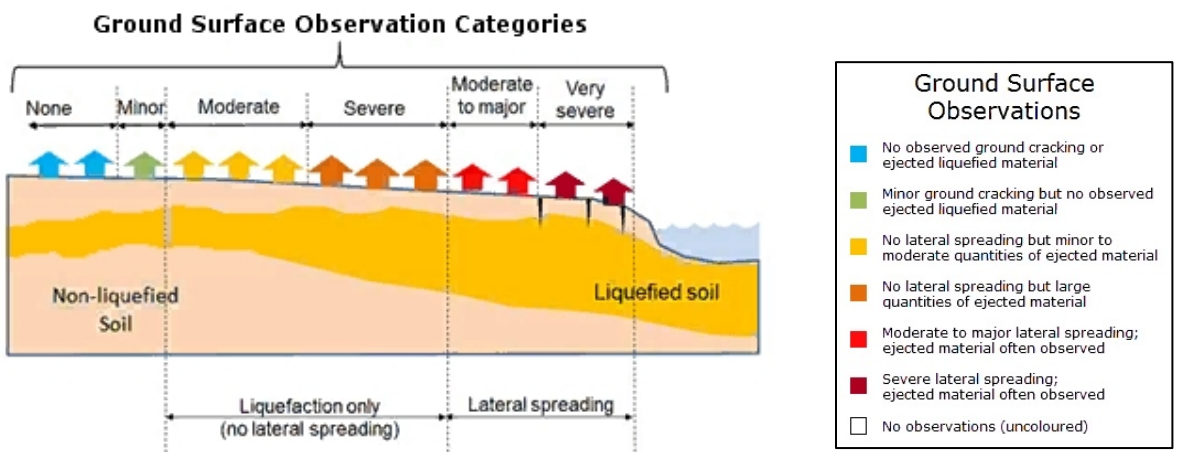

Figure 3.9. Explanation of observation categories (Canterbury Geotechnical Database 2013).

The liquefaction observation map for the area of correlation analysis is shown in Figure 3.10(a) with the four areas of interest identified. The most severe lateral spreading is observed adjacent to the Avon River. Nothing beyond 100-200 m from waterways is mapped as lateral spreading, but large amounts of ejected material are observed further from the river. Figure 3.10(b) shows the amplitudes of displacement measurements from the correlation analysis. Displacements less than the precision threshold were set to zero for visual purposes. Amplitudes are calculated by taking the square root of the sum of the squares of the north/south and east/west displacements (i.e. $\sqrt{(N/S\ disp)^2 + (E/W\ disp)^2}$). The largest displacement amplitudes are represented by purple/blue and are in excess of 3 m.

Figure 3.11 compares the observed liquefaction with the displacement amplitudes from the correlation analysis (bottom) for the Avonside area. Areas of severe lateral spreading (dark red) match with areas of large displacement from the correlation analysis. Most areas where moderate to major lateral spreading were observed correspond to moderate to large displacements. However, the correlation analysis shows some areas of little to no deformation where moderate to major lateral spreading was reported on the observation map. For example, in the area outlined with the dashed circle, little to no deformation is measured in the correlation analysis immediately east of the river; however, the observation map indicates moderate to major lateral spreading. In areas where neither lateral spreading nor large amounts of ejected material were observed, the correlation results show little to no displacement.

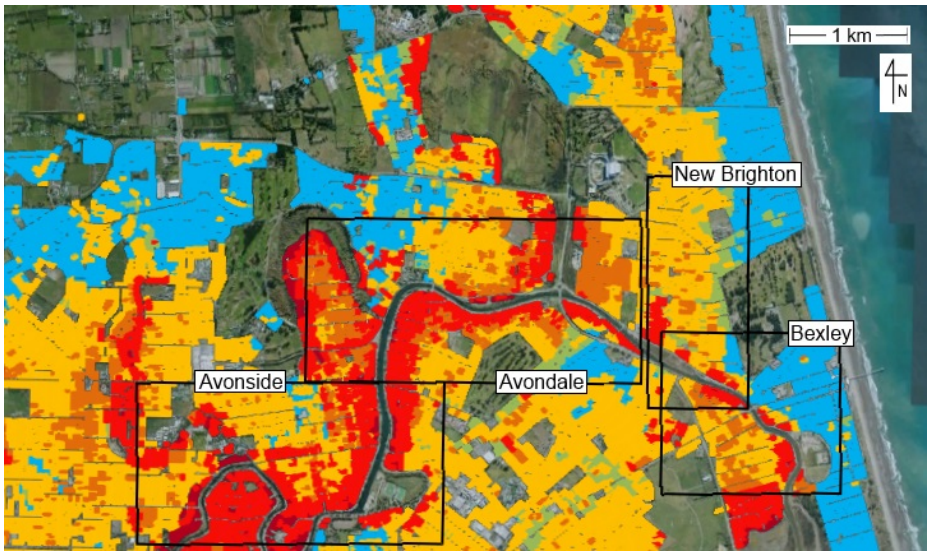

(a)

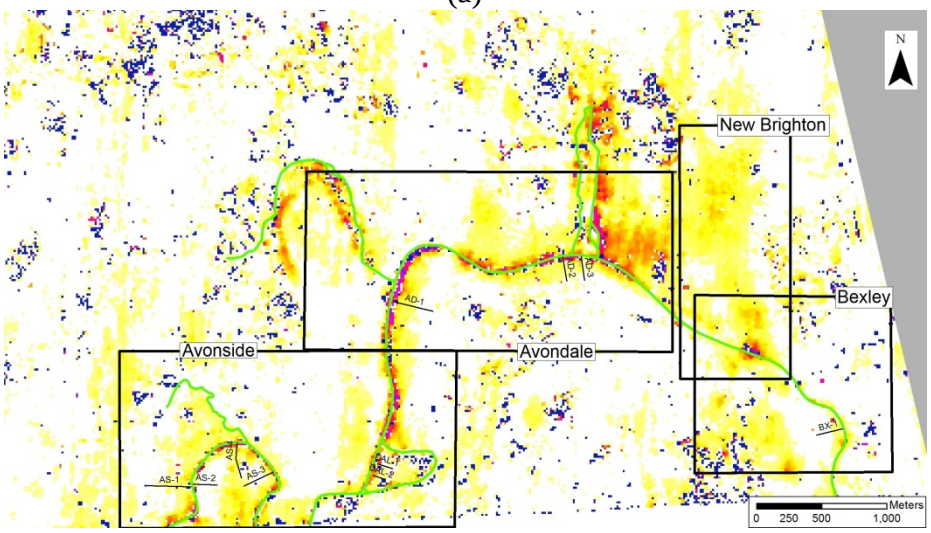

(b)

Figure 3.230. (a) Map of observed liquefaction and lateral spreading (Canterbury Geotechnical Database 2013) and (b) amplitude of displacements from correlation results.

(a)

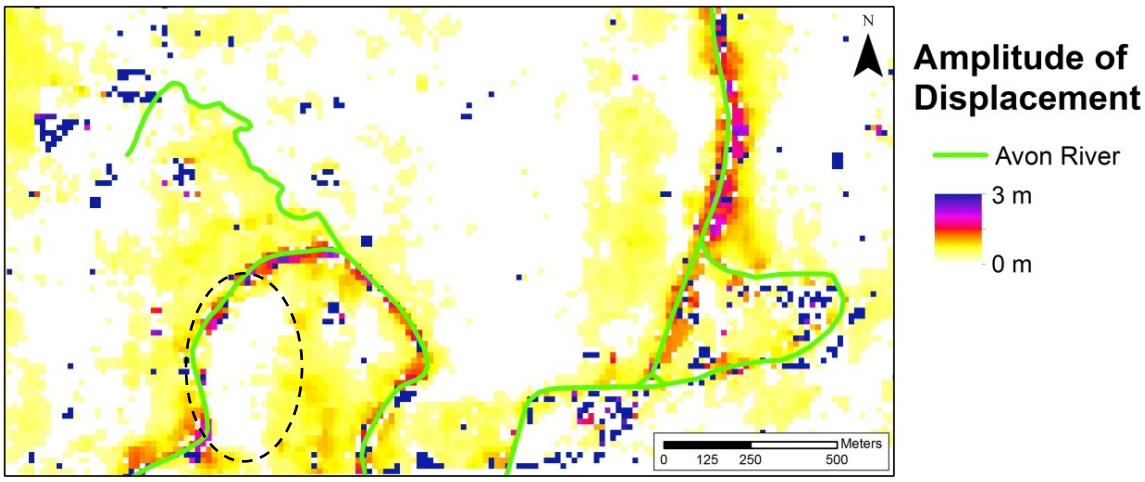

(b)

Figure 3.24. (a) Observations of liquefaction induced deformation (Canterbury Geotechnical Database 2013) and (b) amplitude of displacement measurements in the Avonside area.

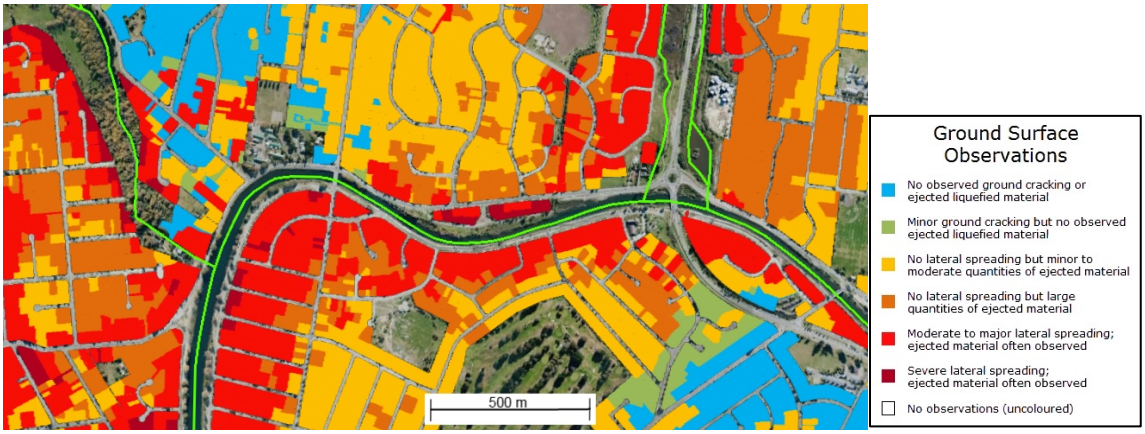

(a)

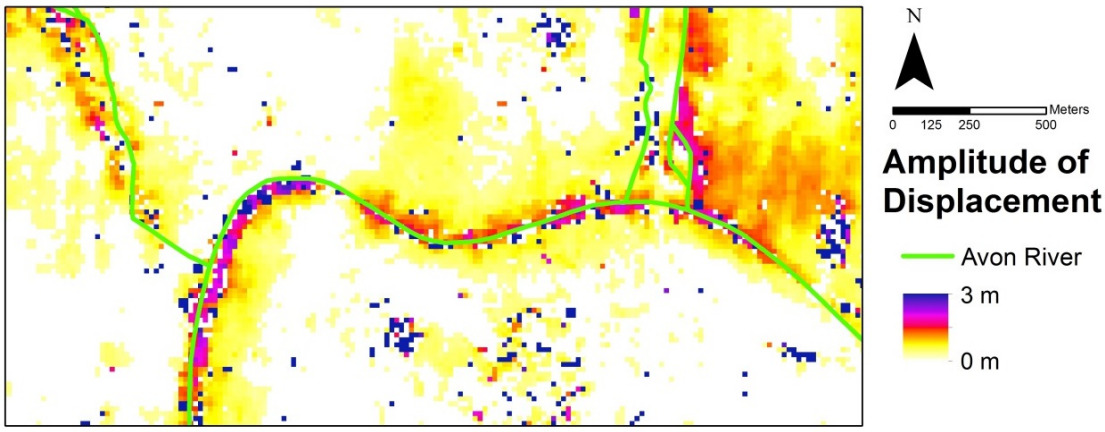

(b)

Figure 3.25. (a) Observations of liquefaction induced deformation (Canterbury Geotechnical Database 2013) and (b) amplitude of displacement measurements in the Avondale area.

The liquefaction observation map and displacement amplitudes from the correlation analysis for the Avondale area are presented in Figure 3.12. The magnitude and extent of displacements match the severity and extent of observations south of the Avon River. However, displacements north of the river in the center of the image and displacements in the northeast of the area shown do not match ground observations. In these areas, the correlation analysis reveals significant lateral deformation which extends further than 200 m from the riverbank, but ground observations record only large amounts of ejected material and no lateral spread deformation 100 m from the river. However, it is possible that any lateral displacement in this area was hidden by the significant ejecta and thus not observed or noted by the field mapping.

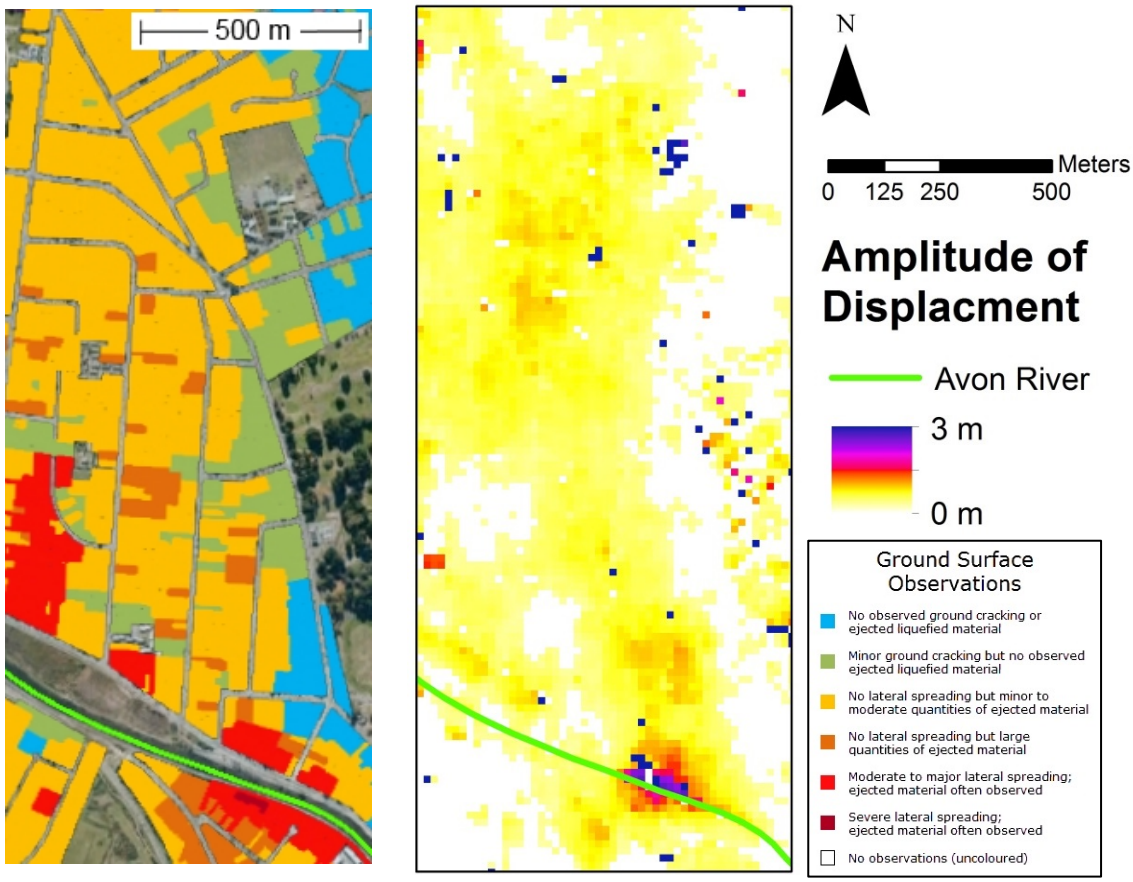

(a) (b)

Figure 3.26. (a) Observations of liquefaction induced deformation (Canterbury Geotechnical Database 2013) and (b) amplitude of displacement measurements in the New Brighton area.

Figure 3.13 shows the liquefaction observations with the displacement measurements from correlation analysis in the New Brighton area. Both ground observations and the correlation results show lateral spreading adjacent to the southeastern part of the river in this area. The ground observations indicate lateral spreading terminates within 100 m of the Avon River. The correlation results south of the river agree with the ground observations on the extent of the lateral spread, but the correlation results indicate the lateral spreading north of the river extends well beyond 100 m. In the center and northern parts of the New Brighton area, the correlation results show widespread deformation of about 1 m. The ground observations note large amounts of ejected material in these areas, but lateral spreading was not reported. However, as discussed for the Avondale area, it is possible that significant ejecta masked any evidence of lateral spreading.

Ground liquefaction observations and correlation displacement results in the Bexley area are presented in Figure 3.14. Ground observations show lateral spreading and ejected material predominately west of the Avon River. Little to no lateral spreading and ejected material are indicated east of the river. The correlation results agree well with these ground observations. East of the river, the correlation results reveal no lateral deformation, but significant deformation was measured on the western banks of the Avon River.

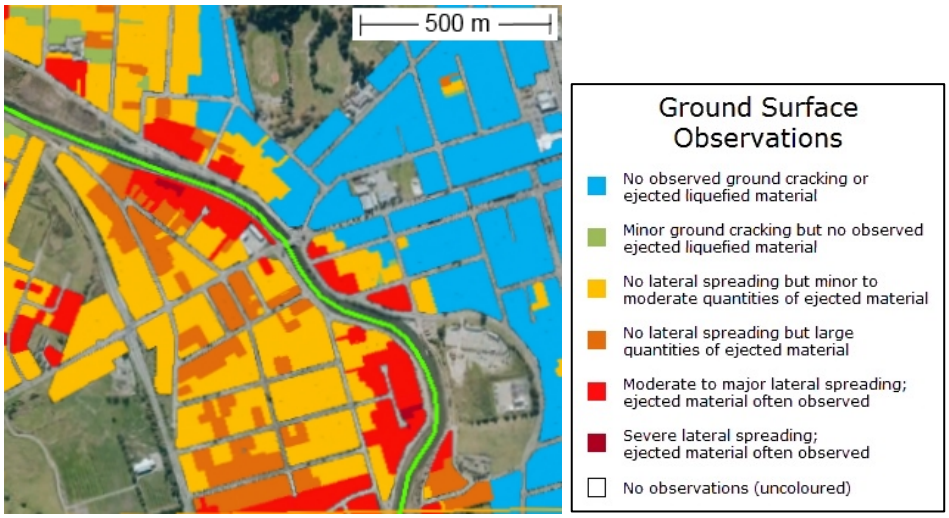

(a)

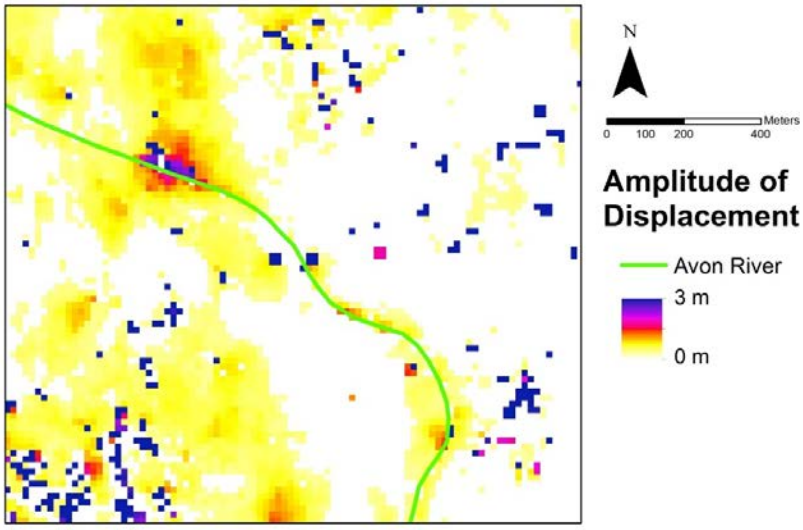

(b)

Figure 3.14. (a) Observations of liquefaction induced deformation (Canterbury Geotechnical Database 2013) and (b) amplitude of displacement measurements in the Bexley area.

Based on the comparisons shown, the qualitative ground observations agree with the correlation results. Areas where ground observations indicate lateral spreading correspond with lateral deformation measured from the correlation analysis. In areas where there is disagreement, the significant ejects may have masked evidence of lateral spreading, and thus it was not reported in the field observation map. The correlation analysis was not as significantly influenced by the ejecta because of the presence of buildings upon which to correlate, and thus the correlation analysis could identify displacements in these areas.

3.3.2 Comparison with Quantitative Lateral Spreading Displacement Measurements

Hundreds of transects of displacement in zones of lateral spreading along the Avon River were measured using traditional methods following the 2011 Christchurch Earthquake (Robinson et al. 2012). These measurements were taken by measuring widths of cracks associated with identified lateral spreading along a linear transect and summing the crack widths to obtain a relationships of the permanent displacement versus distance from the river. Displacements from six transects within the Avonside area were used to compare with the results from optical image correction. All field-measured cracks were assumed to contribute to movement towards the river only. The detailed displacements along the transects were obtained from the University of Canterbury through personal communication with Misko Cubrinovski. For each transect displacements from field measurements and from the correlation analysis are plotted versus distance from the riverbank.

For comparison with the field measurements, displacements along the transects were computed from the correlation analysis by sampling measurements every 10 m along each transect. At each sampling point, the displacement measurements perpendicular to the transect and within 24 m of the transect were averaged to get a representative displacement. An example of the pixels used to estimate displacements along transect AS-1 is shown in Figure 3.15. Each color represents a sampling group of three pixels. From these sampled measurements, both the total displacement amplitude and the displacement perpendicular to the river were computed. The total displacement amplitude is the magnitude of displacement without regard to direction. The displacement perpendicular to the river is the magnitude of the displacement in the direction of the transect and negative values represent movement away from the river. If all displacement is directed along the transect and toward the river, both displacements will be the same. For comparison to the field measurements, displacement perpendicular to the river is more relevant. Transects will be examined individually, and their locations on satellite imagery will be shown. The transect locations are also shown with the north/south and east/west displacement measurements in Figure 3.7 and Figure 3.8.

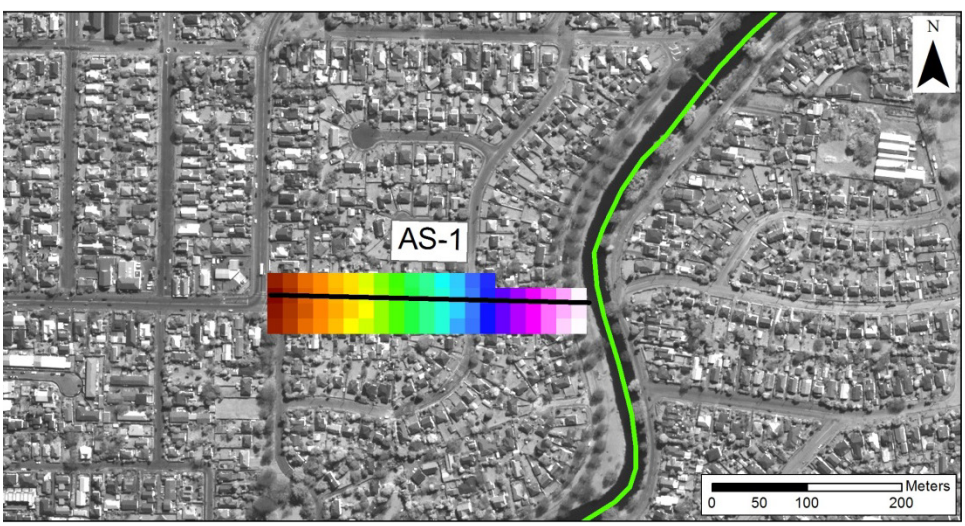

Figure 3.15. Example of transect calculation from correlation results.

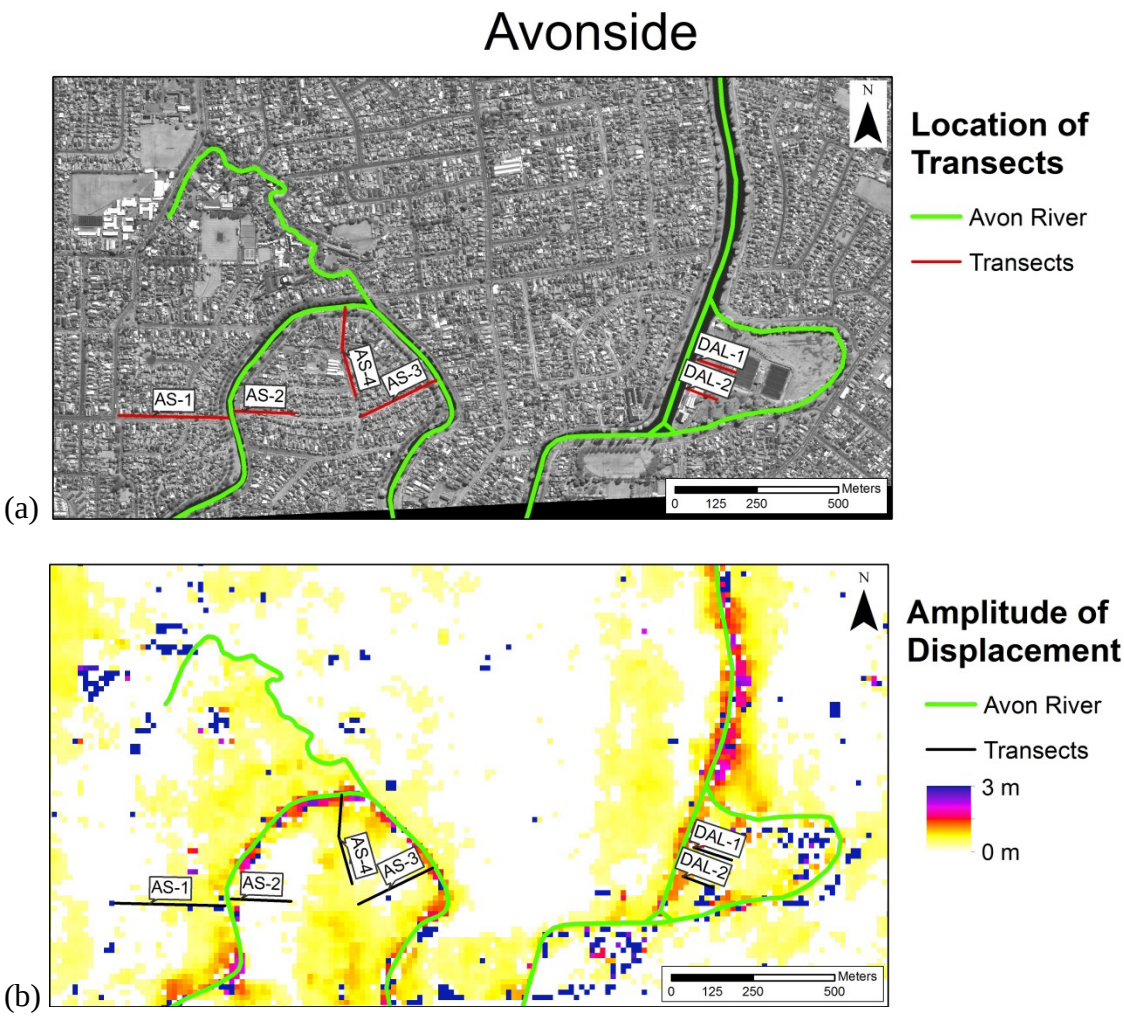

Figure 3.16. (a) Location of transects in the Avonside area and (b) displacement amplitudes from correlation analysis with respect to transect locations.

Figure 3.16 shows the locations of the six transects within the Avonside area and the detailed displacement profiles for these transects are shown in Figures 3.17 and 3.18. Field measurements for AS-1 were collected four months after the Christchurch earthquake on May 20, 2011 by measuring cracks along North Avonside Drive. These cracks were predominately in sidewalks, retaining structures, and road curbs. Cracks in road curbs were only measured where similar cracks appeared on both sides of the street. Also, where the road ended near the river, separation between the asphalt pavement and the street gutter was assumed to be from lateral spreading. Other cracks may have been missed because the street had been repaired at the time of survey. Figure 3.17(a) presents displacement versus distance from the riverbank from the two methods for AS-1. For the correlation analysis, total displacement amplitudes closely follow displacements oriented perpendicular to the river indicating the movement was predominantly towards the river. The correlation results match the ground survey near the river, but beyond 50 m from the river edge the correlation results show larger displacements than ground observations. The lateral spread displacements terminate within 300 m of the riverbank according to the ground survey, but the correlation results indicate movements extend further than 300 m from the river.

Transect AS-2 was measured eastward along the west end of Robson Street on April 7, 2011. Cracks in the street and the top of the riverbank were measured for the ground survey. No other specifics were provided regarding the ground survey. Figure 3.17(b) shows the ground survey measurements with the correlation analysis results. The correlation analysis results show some differences between the total displacement amplitudes and the displacements perpendicular to the river. The negative displacement perpendicular to the river near the river edge may be due to the pixel at the river edge being influenced by displacements from the other side of the river. Note that the displacements for each pixel represent the average across an area of 64 m by 64 m, and thus pixels close to the river extend across the river. It is not clear why other transects were not affected in the same way. The displacements in Figure 3.17(b) agree well over distances of 20 to 100 m from the river.

Transect AS-3 was surveyed along the east side of Robson Street on April 7, 2011. Measured cracks were predominately in the street curbs and sidewalks. Some cracks were difficult to measure as they had been repaired. Some cracks were compressed due to localized uplift. In areas farther from the river, it was unclear if the cracks were associated with lateral spreading or other liquefaction induced deformation (e.g., ground settlement). Figure 3.17(c) shows the displacement measurement from image correlation and the field survey for AS-3. For the correlation analysis, the total displacement amplitude closely matches the displacement perpendicular to the river along the majority of the transect showing most lateral deformation occurred in the direction of the transect. The increase in displacement beyond 150 m from the river shown by the correlation results is likely part of a separate lateral spread which is oriented toward the east (See Figure 3.16(b)). Both the ground survey and correlation analysis indicate lateral spreading along AS-3 terminates around 140 m from the river, and both show the permanent displacement near the river is close to 1 m.

Displacement measurements for transect AS-4 were acquired on March 7, 2011 along Gailbraith Drive. Cracks in the street, curb, and sidewalk were measured, and cracks in the curb were only measured if similar cracks could be found on both sides of the street. Some cracks were partially filled with sand, and the cracks after the shift in the street were transposed onto an ideal transect in a graphical information system (GIS). Figure 3.17(d) shows the measured displacements versus distance from the river. Correlation results show most of the measured displacement occurred toward the river. Both the ground survey and correlation results suggest the permanent displacement at the riverbank is close to 1.5 m, and both match in their distribution of permanent displacements with respect to distance from the river. The ground survey indicates that the lateral spread displacements terminate around 220 m from the riverbank, but the correlation analysis suggests the lateral spread terminates about 250 m from the river.

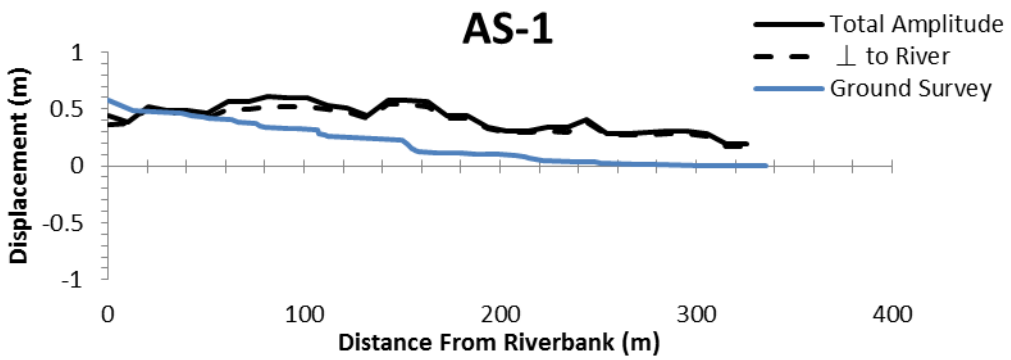

(a)

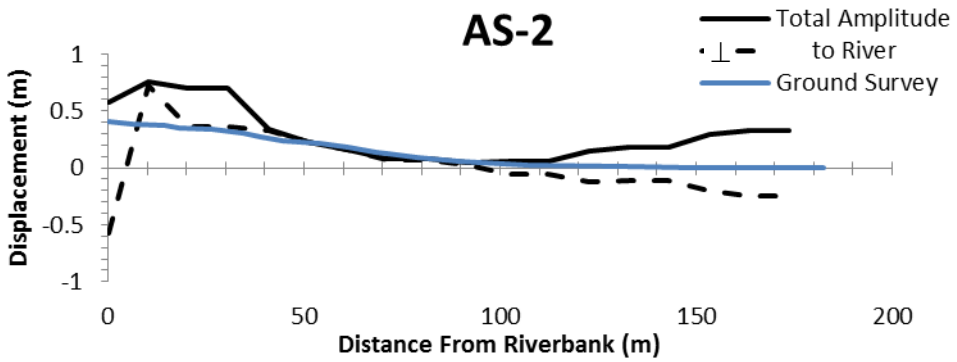

(b)

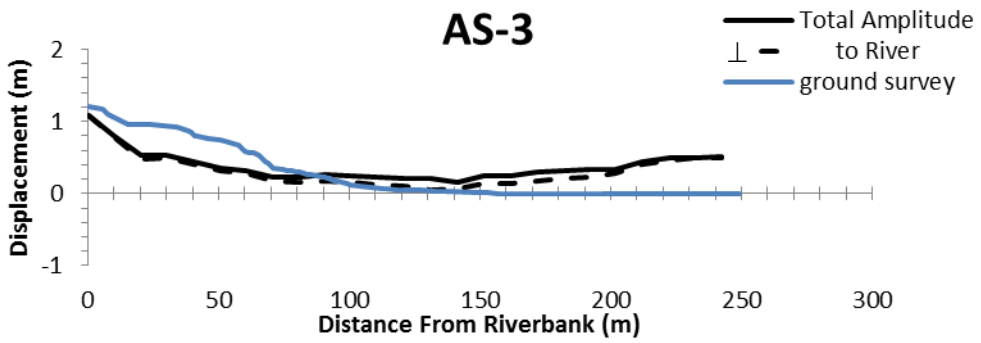

(c)

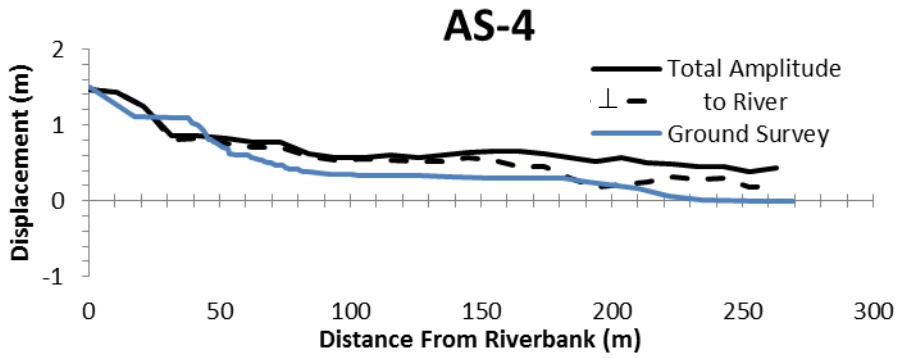

(d)

Figure 3.17. Comparison of displacement measurements from transects AS-1 through AS-4

Measurements for transect DAL-1 were collected in Porrit Park on March 2, 2011. Cracks were found in the grass, footpath, and parking lot. Some areas in the grass exhibited a graben structure, making measurements difficult. All observed cracks were thought to contribute to lateral spreading moving to the west. Figure 3.18(a) shows the measured displacements with respect to distance from the river. Within 40 m, the correlation results indicate most of the movement is in the direction of the transect, but displacement beyond 40 m may be due to lateral spreading towards the creek to the south and east (see vectors in Figure 3.25). When compared with the ground survey measurements, the correlation results are very different. The correlation results indicate that lateral spreading terminates abruptly at 40 m, but the ground survey indicates lateral spreading displacements continue to about 70 m from the river. Additionally, permanent displacement measurements at the riverbank differ by more than 1 m. Cubrinovski (personal communication) suggested differences may be explained in part by the assumption that all cracks contributed to movement toward the river along the measured transect. This explanation is supported by the correlation displacement vectors in Figure 3.16 that show movement towards the east within the park. Differences may be further influenced by poor performance of correlation analyses in fields that do not have significant tonal variation upon which to correlate. This makes the displacement estimates more uncertain in these areas.

Transect DAL-2 was measured on March 2, 2011. Cracks in pavement, concrete, and a gravel lot were measured. Many cracks were filled with sand, and a line of sand boils was observed near 50 m from the river. Cubrinovski and his students also noted that cracks from settlement were difficult to distinguish from cracks due to the lateral spreading, and that southward lateral spreading occurred near the end of the DAL-2 transect. These challenges caused much difficulty in field measurement of the lateral spread. Figure 3.18(b) shows the distribution of displacements along DAL-2. Correlation results show that most movement is towards the river within 20 m of the riverbank. Ground survey results match the correlation results moderately well. Both methods show the lateral spreading displacement terminating within 50 m of the river, and the distribution of displacement is similar throughout. Permanent displacements at the river edge are from 1.0-1.5 m. Differences in measurements can be explained by the difficulty of ground measurements and the challenges of correlation analyses in grassy areas.

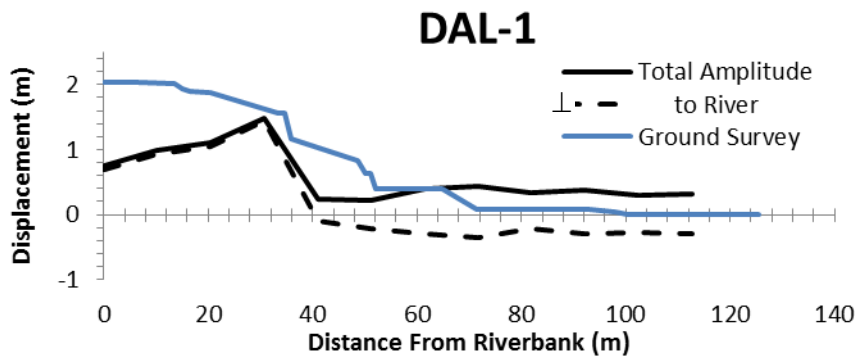

(a)

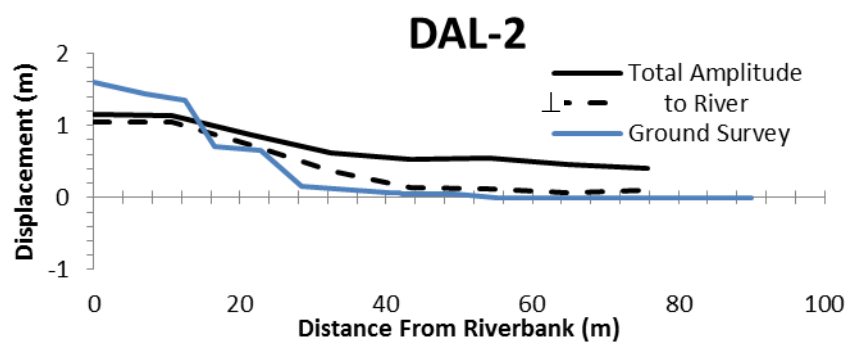

(b)

Figure 3.18. Comparison of displacement measurements from transects DAL-1 and DAL-2.

4.0 OPTICAL IMAGE CORRELATION ANALYSIS OF LIQUEFACTION FROM THE 2011 TOHOKU, JAPAN EARTHQUAKE

4.1 Study Area

On March 11, 2011, a magnitude 9.0 (M_w) megathrust earthquake struck off the coast of Japan. This earthquake was the fifth largest ever recorded and caused more than 20,000 deaths and an estimated $210 billion in damages (Pradel et al. 2014). Although many of the casualties and damage were directly related to the tsunami caused by the earthquake, observed damage along the Tone River was primarily due to liquefaction and lateral spreading. Specifically, severe lateral spreads were observed in the town of Katori along the Tone River (Pradel et al. 2014). It is for this reason that Katori was selected for study. Figure 4.1 shows the location of the earthquake fault rupture relative to the study area around Katori (green box), and the photos in Figure 4.2 represent some lateral spreading damage observed in Katori.

The Tone River flows through a deep sedimentary basin which has been shown to amplify strong motions in past earthquakes (Pradel et al. 2014). Due to anthropogenic adjustments of the Tone River, parts of Katori rest upon former river channels of the Tone River (Pradel et al. 2014). Deposition of these materials is estimated to have occurred less than 500 years ago. Coupled with a shallow water table, coarse grained materials in Katori allow favorable conditions for liquefaction to occur. However, older coarse grained materials far from Tone River are thought to have become resistant to liquefaction.

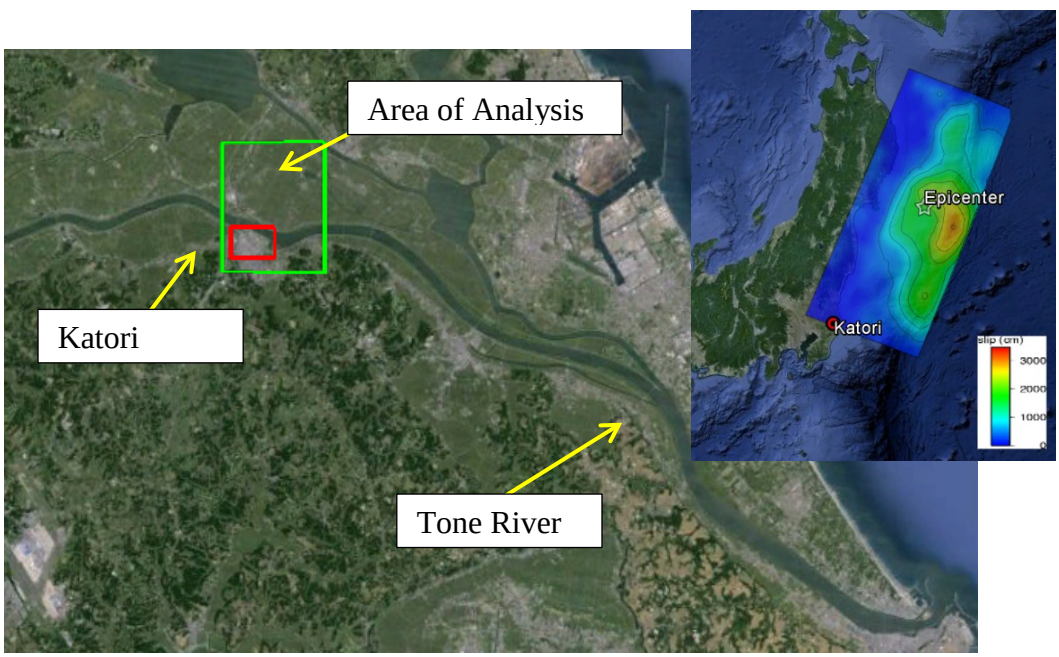

Figure 4.27. Location of Tohoku earthquake fault rupture from Wei et al. (accessed 2014) and the Katori study area shown on Google Earth image (2014).

Figure 4.28. Photos showing damage from lateral spreading in Katori, Japan (Ashford et al. 2011).

4.2 Image Selection and Processing

Based on reports of liquefaction-induced deformation around the town of Katori and availability of satellite imagery, panchromatic (i.e. grayscale) 0.5-m resolution images from WorldView-1 were selected from before the earthquake (December 24, 2010) and after the earthquake (December 11, 2011). Figure 4.3 shows the pre-event satellite image used in the correlation analysis with Katori outlined in red. This area consists of the populated Katori area to the south of the river, agricultural fields north of the river, and some hills to the south of

Katori. The acquisition geometry was agreeable in the two images with the pre- and post-event images having target azimuth angles of 15.1° and 15.4° and off-nadir angles of 13.3° and 11.7°, respectively.

By using equations 2.1, 2.2, and 2.3 and assuming a pseudo-suborbital path of 0° (i.e. $\theta_0 = 0$), north/south look angles (T) of 12.86° and 11.29° and east/west look angles (S) of 3.52° and 3.14° can be established for both the pre- and post-event image, respectively. The difference in the north/south look angles is 1.57°, and the difference in the east/west look angles is 0.38°. Since these differences are small for both directions, significant noise is not expected to occur from differences in acquisition angles.

Images were orthorectified with ENVI software (ENvironment for Visualizing Images, ENVI 2014) using a 90-m resolution digital elevation model (DEM) from the Shuttle Radar Topography Mission (SRTM, USGS 2004). Tie points were automatically generated using ENVI, and tie points were assessed in the same way as presented in previous chapters. Points within 200 m of major waterways were removed, and points with high residuals relative to the warping polynomial were excluded from use in co-registration. Ultimately, 2,272 tie points (77 points per km^2) with an RMSE of 0.30 m with respect to the warping polynomial were selected for co-registration. Figure 4.4 shows the tie points selected for use in co-registration with their residuals from the warping polynomial represented by color. Notice the larger density of tie-points identified south of the river in the populated areas, where there are more features upon with to identify tie-points. It was more difficult to identify a large number of tie points in the agricultural fields to the north of the river.

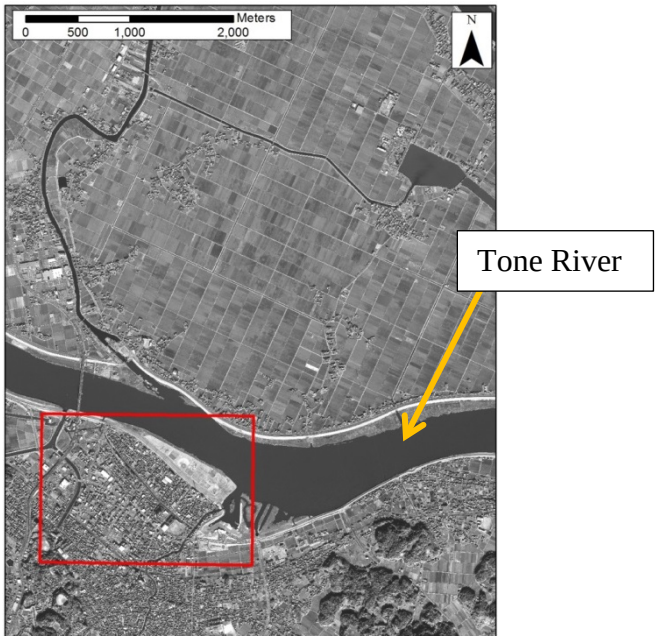

Figure 4.29. Pre-earthquake image; Katori outlined in red.

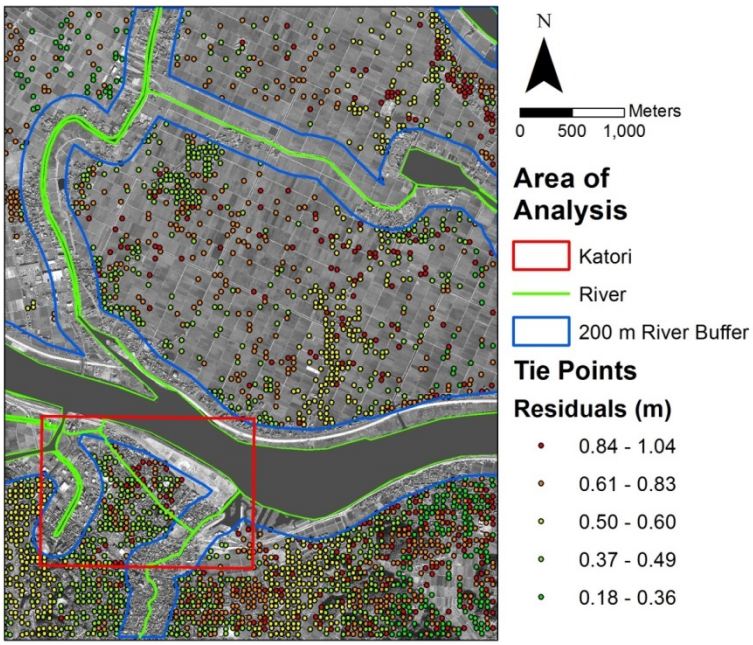

Figure 4.30. Tie points used in co-registration.

Following co-registration, correlation analysis was performed using the method presented by Leprince et al. (2007). A window size of 256 pixels (128 m) was used with a step size of 64 pixels, producing a displacement measurement every 32 m. This window size is larger than used in the analyses for Christchurch because the area around Katori is predominately used for agriculture and has homogenous texture. Results were filtered such that measurements with a signal-to-noise ratio (SNR) less than 0.95 were designated "decorrelated". A precision threshold of 0.30 m was established from the co-registration RMSE.

4.3 Deformation Results

Displacement measurements of horizontal deformation were calculated for the north/south and east/west directions. Figure 4.5 presents the north/south displacements in the region of study. Displacements less than the precision threshold (0.30 m) were set to zero for visual purposes. Northward movements are represented by yellow/red with red indicating displacements in excess of 2 m. Similarly, southward movement is represented by blue/purple with purple indicating displacements in excess of 2 m. In Katori (red box), coherent zones of horizontal deformation are indicated. The southern riverbank of the Tone River displaced northward, while areas on the north side of the small canal running through the middle of the town of Katori displaced southward. Additionally, areas adjacent the tributary north of Katori show large displacement. Areas far from the Tone River and major waterways show little to no coherent horizontal deformation.

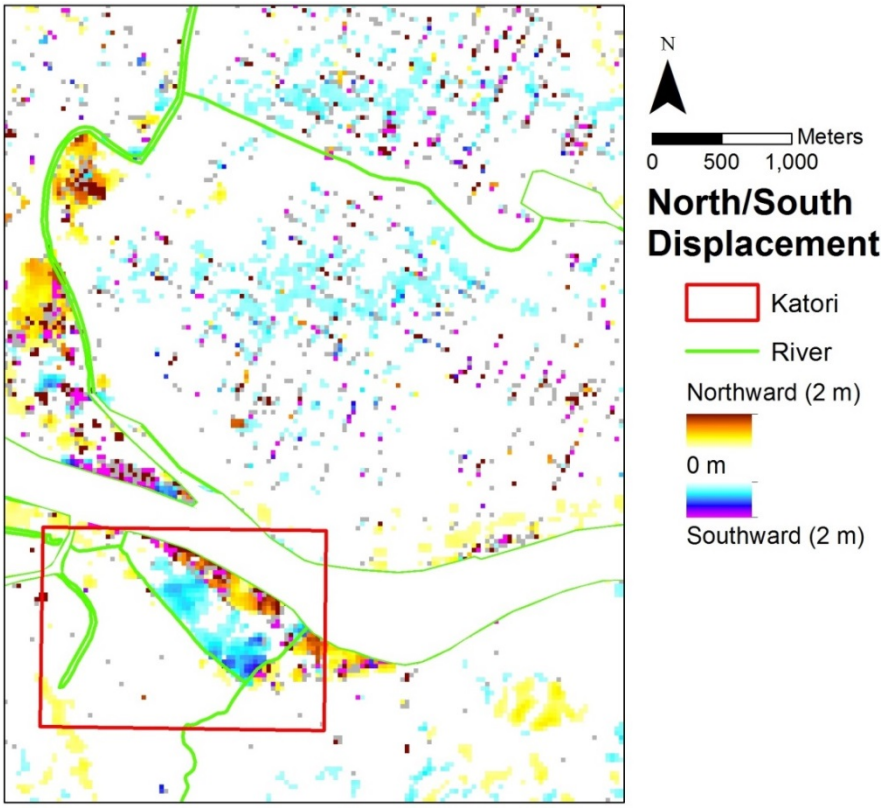

Figure 4.31. North/south displacements from correlation analysis.

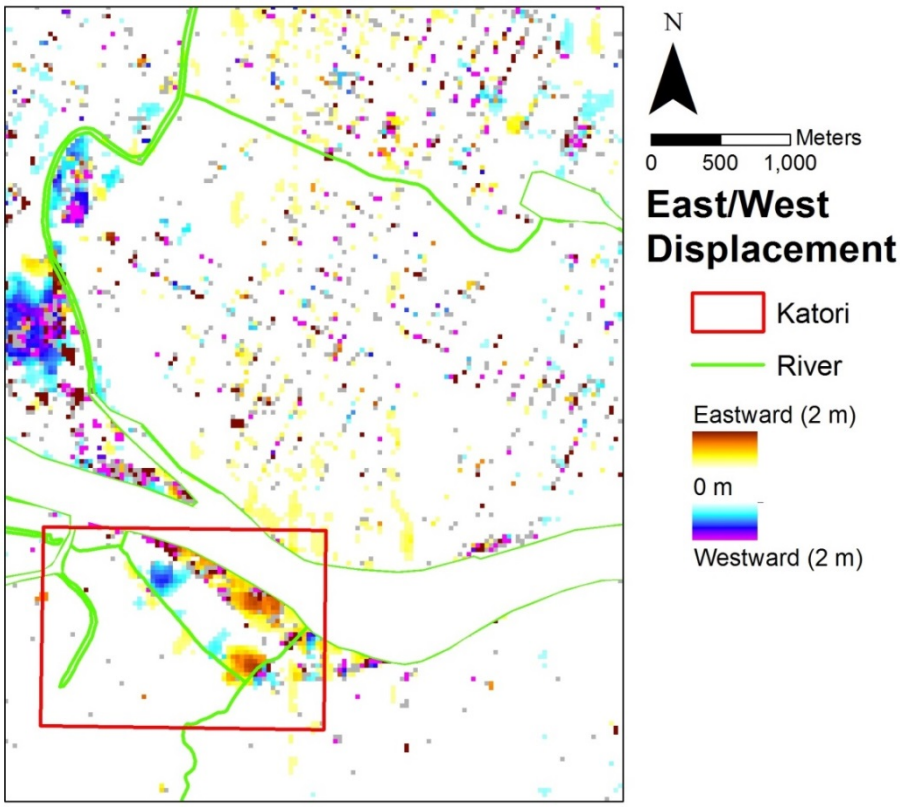

Figure 4.32. East/west displacements from correlation analysis.

Figure 4.6 presents the measured displacements in the east/west direction. Displacements less than the precision threshold (0.30 m) were set to zero for visual purposes. Again, coherent deformation patterns are seen in Katori between the canal running through the middle of Katori and the Tone River. The southern riverbank of the Tone River displaces eastward, which is consistent with displacement perpendicular to the river where the river is slightly oriented northwest/southeast. For the canal running through the town of Katori, displacements toward the west are measured along one section towards the canal's western end. Near its eastern end where the canal meets a stream flowing to the north, eastward displacement toward the stream is observed. To the north of the Tone River in the western part of the image, a coherent pattern of large displacement is oriented westward, away from the tributary. In areas far from major waterways, little to no displacement is measured.

4.3.1 Comparison with Former River Channel

Although the Tone River flows near Katori today, it has not always done so. Beginning in the 1600s, many canals were constructed and river channels diverted to facilitate trade to Tokyo (Pradel et al. 2014). During this time, the path of the Tone River was altered such that it flowed eastward into the Pacific Ocean. This alternation is responsible for much of the loose sediment fill placed in and around present-day Katori.

Figure 4.7 compares the shoreline from the 1880s with satellite imagery of the area today and the displacement amplitudes from the correlation analysis. Today, much of Katori rests upon the former path of the Tone River, as indicated by the location of the 1880s shoreline shown in Figure 4.7(a). Consequently, much of Katori is susceptible to liquefaction (and thus lateral spreading). Figure 4.7(b) shows the displacement amplitudes from the correlation analysis superimposed on the Google earth image that shows the 1880s shoreline. The displacement amplitudes were calculated by taking the square root of the sum of the squares of the directional displacements (i.e., $\sqrt{NS^2 + EW^2}$), and measurements less than the precision threshold were not included for visual purposes. Significant displacement is well bounded by the former shoreline of the Tone River with nearly all lateral spreading occurring within the location of the former river channel. Therefore, displacement measurements qualitatively agree that lateral spreading occurred within these areas most susceptible to liquefaction and lateral spreading.

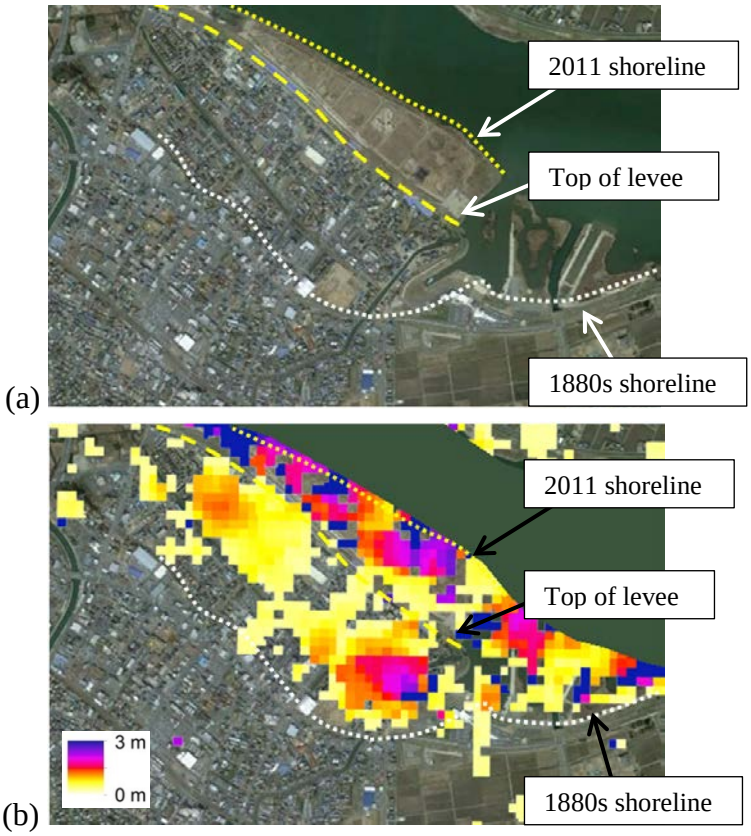

Figure 4.33. (a) Shoreline from the 1880's from Pradel et al. (2014) superimposed on present-day satellite image and (b) displacement amplitudes from correlation analysis superimposed on satellite image (Google Earth 2014).

4.3.2 Comparison with Displacement Observations

From personal communication with Teruo Nikai, Professor of Civil Engineering at the Nagoya Institute of Technology in Japan, measurements of liquefaction-induced horizontal deformation in Katori were obtained. These measurements were collected for the city of Katori and were used to study liquefaction countermeasures. Measurements were digitized and rendered as vectors scaled 1:50 (i.e. an arrow of 50 m length represents 1 m of horizontal displacement). Displacements from the correlation analysis were also rendered as arrows scaled 1:50 for visual comparison. Displacements below the precision threshold (0.30 m) are excluded for visual clarity.

Measurements are presented in two areas for ease of comparison. Figure 4.8 displays the locations of the two areas. Vectors in the area outlined in black are shown in Figure 4.9(a) along with the location of the canal. North of the canal, displacements from both sources agree in magnitude (~ 1 m) and direction (south and southwest). South of the canal, vectors from ground measurements are oriented northward toward the canal, but vectors from the correlation analysis are oriented southward. This difference may be due to smoothing effects in the correlation analysis due to the use of a large correlation window (128 m by 128 m). Vectors in the area outlined in yellow in Figure 5.9 are presented in Figure 4.9(b). Vectors are more agreeable in this area. Displacements from both sources have similar magnitude and direction (eastward).

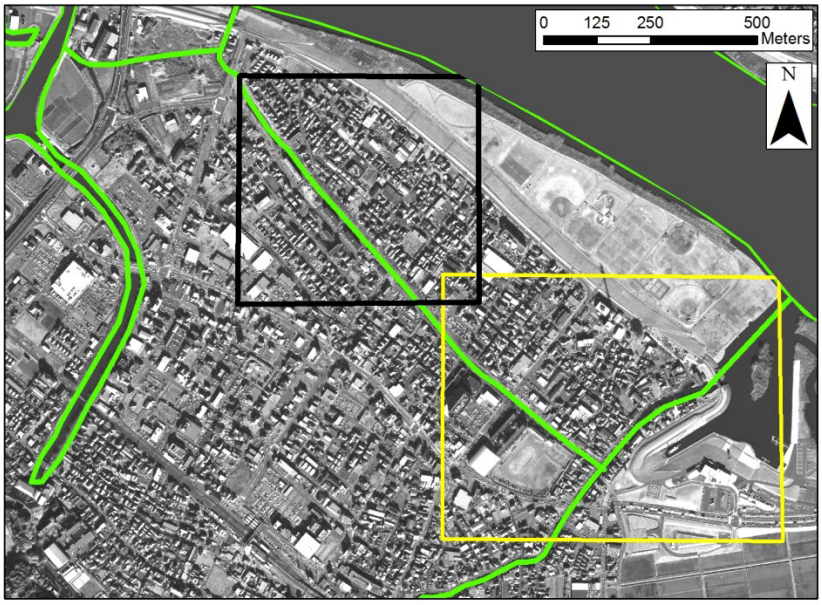

Figure 4.34. Locations of areas of comparison within the town of Katori.

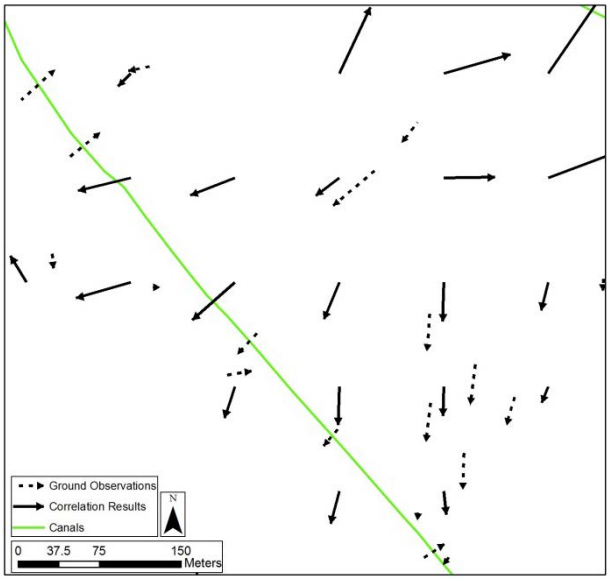

(a)

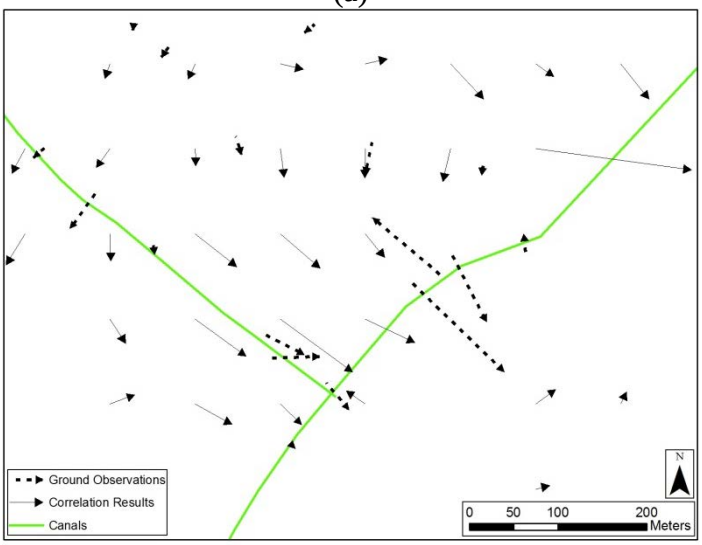

(b)

Figure 4.35. Displacement vectors from ground surveys by the City of Katori (personal communication with Teruo Nikai) and correlation analysis in (a) western Katori and (b) eastern Katori. Vectors scaled 50:1

5.0 CONCLUSIONS

Liquefaction-induced deformations associated with lateral spreading represent a significant earthquake hazard that can cause substantial damage during earthquakes. The ability to accurately predict lateral-spreading displacement is hampered by a lack of field data from previous earthquakes. Remote sensing via optical image correlation can fill this gap and provide data regarding liquefaction-induced lateral spreading displacements.

Liquefaction-induced horizontal deformations were measured using optical image correlation. Specifically, 0.5-m resolution, panchromatic satellite image pairs were analyzed for two earthquakes, the 2011 Christchurch Earthquake in New Zealand and the 2011 Tohoku Earthquake in Japan. The Christchurch Earthquake was analyzed first because the liquefaction was well-documented and the field data helped in our understanding of the remote sensing results. Subsequently, the area around the city of Katori was analyzed for the 2011 Tohoku Earthquake. For each study area, the deformations from optical image correlation were compared with ground observations of liquefaction and its effects.

For the Christchurch earthquake, optical image correlation was applied to the neighborhoods along the Avon River to the northeast of the Christchurch Central Business District. Horizontal deformation patterns from optical image correlation were concentrated around the Avon River. Most displacement patterns occurred within 300 m of the Avon River, but some coherent patterns extended beyond 500 m from the riverbank, specifically in the Avondale and New Brighton areas. Comparing the displacements from the correlation analysis with field observations, areas with large displacements generally occurred in areas with observed lateral spreading. Deformation patterns that extended far beyond the Avon River were typically contained within areas of observed liquefaction. Ground survey measurements along transects were quantitatively compared to measurements from optical image correlation. While the degree and nature of similarity between the ground survey measurements and those from image correlation differed in each transect, measurements along most transects were agreeable.

For the Tohoku earthquake, the town of Katori along the Tone River was analyzed. Displacement patterns from the optical image correlation analysis were concentrated on the southern riverbank of the Tone River in the town of Katori and north of the canal which runs parallel to the Tone River and through the town of Katori. Little to no displacement was measured far from the Tone River and other major waterways. Comparison of the correlation results with the historical path of the Tone River revealed that nearly all coherent patterns of displacement occurred within the land reclaimed from the Tone River. Correlation results were also compared to measured horizontal deformation patterns in the town of Katori collected for the City of Katori. Correlation results generally agreed with horizontal deformation measurements in both direction and magnitude.

Overall, the displacement patterns from optical image correlation compared favorably with all sources of comparison for both earthquakes. Correlation results matched sources of comparison better in areas with more features or heterogeneous texture (e.g. urban areas) than in areas with few features and homogeneous texture (e.g. agricultural fields). Typically, large-scale displacement patterns were more easily discernable in the correlation results than in other sources of lateral spreading measurements.

While a sub-pixel precision threshold (i.e., less than 0.5 m) was achieved for all correlation analyses, many factors contributed the quality of correlation results. Agreement of acquisition angles between the two images being analyzed had the greatest effect on the correlation results. Where acquisition angles differed more significantly, false matches were more likely to occur

during the correlation process, and thus, the displacement results tended to have more noise. Co-registration errors largely controlled the precision of measurements. Specifically, the RMSE of the tie points with regard to the warping polynomial dominated other sources of error, and this RMSE was found to be a reliable predictor of measurement precision. Tie points were more easily identified in areas with many features or heterogeneous texture. For example, more tie points tended to be generated in urban areas than in agricultural fields.

In addition to tie point generation, the correlation process was affected greatly by the texture of the area. False matches were more likely in areas with few features and homogeneous texture. Thus, the correlation process performed more reliably in areas with many features and heterogeneous texture. Additionally, false matches were more common when a smaller correlation window was used because fewer distinguishable features were encompassed in the correlation window. Thus, analyses with a smaller correlation window produced more noise than with a larger window. However, a trade-off exists in correlation window size. Displacements from correlation analysis were somewhat averaged or smoothed over the correlation window. If a large correlation window encompassed areas that displaced both a large amount and a small amount, the correlation analysis would yield a displacement measurement in between the two displacement magnitudes. Therefore, to measure more localized/discrete deformation patterns a smaller correlation window is required. Thus, the smallest correlation window which produces an acceptable level of noise was preferred.

REFERENCES

Ashford, Scott A., Ross W. Boulanger, Jennifer L. Donahue, and Jonathan P. Stewart. *Geotechnical Quick Report on the Kanto Plain Region during the March 11, 2011, Off Pacific Coast F Tohoku Earthquake Japan*. Rep. no. GEER-025a. N.p.: Geotechnical Extreme Events Reconnaissance (GEER), Apr. 2011.

Bethel, J. Purdue University, n.d. Web. 20 Feb. 2014. <https://engineering.purdue.edu/~bethel/elem3.pdf>.

Binet, R. and L. Bollinger. "Horizontal Coseismic Deformation of the 2003 Bam (Iran) Earthquake Measured from SPOT-5 THR Satellite Imagery." *Geophysical Research Letters* 32.2 (2005).

Bukata, R. P. Optical Properties and Remote Sensing of Inland and Coastal Waters. Boca Raton, FL: CRC, 1995. 76-79. Print.

Caee.utexas.edu. "Evaluation of Integrated Seismic Hazards & Ground Failure in Pull-Apart Basins during The Izmit Earthquake In Turkey." Web. 13 Dec. 2013. http://www.caee.utexas.edu/prof/rathje/research/turkey.html

Canterbury Geotechnical Database (2012) "Horizontal Ground Surface Movements", Map Layer CGD0700 - 23 July 2012, retrieved Feb 15 2014 from https://canterburygeotechnicaldatabase.projectorbit.com/

Canterbury Geotechnical Database (2013) "Liquefaction and Lateral Spreading Observations", Map Layer CGD0300 - 11 Feb 2013, retrieved Feb 15 2014 from https://canterburygeotechnicaldatabase.projectorbit.com/

Casson, B., C. Delacourt, D. Baratoux, and P. Allemand. "Seventeen Years of the "La Clapière" Landslide Evolution Analysed from Ortho-rectified Aerial Photographs." *Engineering Geology* 68.1-2 (2003): 123-39. Print.

Cubrinovski M, Bradley B, Wotherspoon L, Green R, Bray J, Wood C, Pender M, Allen J, Bradshaw A, Rix G, Taylor M, Robinson K, Henderson D, Giorgini S, Ma K, Winkley A, Zupan J, O'Rourke T, DePascale G, Wells D. "Geotechnical aspects of the 22 February 2011 Christchurch earthquake." *Bulletin of the New Zealand Society for Earthquake Engineering* 44.4 (2011): 205-226.

Debella-Gilo, Misganu, and Andreas Kääb. "Measurement of Surface Displacement and Deformation of Mass Movements Using Least Squares Matching of Repeat High Resolution Satellite and Aerial Images." *Remote Sensing* 4.1 (2012): 43-67. Print.

EERI. "The M W 7.0 Haiti Earthquake of January 12, 2010: Report #1." EERI Special Earthquake Report April. 2010 Web.

EXELIS. "Warp and Resample." *Warp and Resample (Using ENVI) | Exelis VIS Docs Center*. N.p., n.d. Web. 23 Aug. 2013. <http://www.exelisvis.com/docs/warpingresampling.html>.

ENVI version 4.8. Exelis Visual Information Solutions, Boulder, Colorado. Used 2014.

Gao, Feng, Jeffrey Masek, and Robert E. Wolfe. "Automated Registration and Orthorectification Package for Landsat and Landsat-like Data Processing." *Journal of Applied Remote Sensing* 3.1 (2009)

GDAL. 2012. GDAL - Geospatial Data Abstraction Library: Version 1.9.2, Open Source Geospatial Foundation, http://gdal.osgeo.org

Google Earth (Version 7.1.2.2041), accessed 2014.

Hamada, M., I. Towhata, S. Yasuda, and R. Isoyama. "Study on Permanent Ground Displacement Induced by Seismic Liquefaction." Computers and Geotechnics 4.4 (1987): 197-220. Print.

Krause, Keith S. "WorldView-1 Pre and Post-launch Radiometric Calibration and Early On-orbit Characterization." Proc. of SPIE 7081 (2008)

Leprince, S., S. Barbot, F. Ayoub, and J. Avouac. "Automatic and Precise Orthorectification, Coregistration, and Subpixel Correlation of Satellite Images, Application to Ground Deformation Measurements." IEEE Transactions on Geoscience and Remote Sensing 2007.

Pradel, Daniel, Joseph Wartman, and Binod Tiwari. "Impact of Anthropogenic Changes on Liquefaction along the Tone River during the 2011 Tohoku Earthquake." *Natural Hazards Review* 15.1 (2014): 13-26. Print.

Puymbroeck, Nadège Van, Rémi Michel, Renaud Binet, Jean-Philippe Avouac, and Jean Taboury. "Measuring Earthquakes from Optical Satellite Images." *Applied Optics* 39.20 (2000): 3486. Print.

Robinson, K., Cubrinovski, M., & Bradley, B. "Lateral Spreading Measurements from the 2010 Darfield and 2011 Christchurch Earthquakes". Paper presented at the Australia New Zealand Conference on Geomechanics (ANZ), Melbourne, Australia. (2012).

Robinson, K., M. Cubrinovski, P. Kailey, and R. Orense. "Field Measurements of Lateral Spreading following the 2010 Darfield Earthquake." *Proceedings of the Ninth Pacific Conference on Earthquake Engineering* Apr. 2011: 52-60.

Suncar, Oscar E., Ellen M. Rathje, and Sean M. Buckley. "Deformations of a Rapidly Moving Landslide from High-Resolution Optical Satellite Imagery." *Geocongress* (2013).

USGS. Shuttle Radar Topography Mission, 3-arc second scene s44_e172_3arc_v1, Version 1.0 2004. Data available from the U.S. Geological Survey at eros.usgs.gov

Wei, Shengji, Anthony Sladen, and ARIA Group. "Slip-History Database :: 2011 Tohoku-oki Earthquake." *2011 Tohoku-oki Earthquake*. Caltech, n.d. Web. 28 Apr. 2014. <http://www.tectonics.caltech.edu/slip_history/2011_taiheiyo-oki/>.